Vilnius University
Faculty of Physics
Institute of Applied Electrodynamics and Telecommunications

Ingrida Pliaterytė

# LOW-FREQUENCY NOISE CHARACTERISTICS OF GRAPHENE-BASED JUNCTIONS AND TRANSISTORS

Master‘s final thesis

Electronics and Telecommunication
Technologies study program

| | |
|---|---|
| Student | Ingrida Pliaterytė |
| Approved | 2026-05-22 |
| Academic supervisor | dr. Justinas Glemža |
| Director of the Institute | prof. Robertas Grigalaitis |

Vilnius 2026

Vilniaus universiteto
Fizikos fakulteto
Taikomosios elektrodinamikos ir telekomunikacijų institutas

Ingrida Pliaterytė

# GRAFENO SANDŪRINIŲ ĮTAISŲ IR TRANZISTORIŲ ŽEMADAŽNIO TRIUKŠMO CHARAKTERISTIKOS

Magistrantūros studijų baigiamasis darbas

Elektronikos ir telekomunikacijų technologijų
studijų programa

| | |
|---|---|
| Studentė | Ingrida Pliaterytė |
| Leista ginti | 2026-05-22 |
| Darbo vadovas | dr. Justinas Glemža |
| Instituto direktorius | prof. Robertas Grigalaitis |

Vilnius 2026

# Table of Contents

# Introduction

Two decades after it was first isolated, graphene remains one of the most extensively studied materials as it exhibits exceptional behavior in terms of its electrical, thermal, mechanical, and optical performance. Due to attractive properties, graphene field effect transistors (gFETs) are used in circuits such as high-speed analog circuits, radio frequency devices (e.g., frequency doubler or multiplier), sensors – gFET-based DNA or gas sensors [1]. Meanwhile, graphene/Si junctions are currently explored for potential applications as solar cells, photodetectors, barristors, and gas sensors [2]. Direct and catalyst-free deposition of graphene on silicon substrates by plasma-enhanced chemical vapor deposition (PECVD) benefits in avoiding time-consuming transfer procedures and reducing the risk of graphene contamination and mechanical damage, and can be easily implemented for large-scale industrial applications. However, such graphene is prone to exhibit structural defects such as grain boundaries, vacancies, or various on-site defects that significantly affect charge transport behaviour in graphene-based devices [3]. Graphene defectivity is one of the reasons for the much lower charge-carrier mobility observed in gFETs [4]. Graphene-based junctions still face unresolved issues such as a large variation of the ideality factor, a wide distribution of Schottky barrier height, and limited performance due to various interface defects, such as dangling bonds at the silicon surface [5]. Thus, further research is needed.

Low-frequency noise measurements are employed for the investigation of such graphene-based devices as a sensitive and non-destructive tool for assessing their defectiveness, evaluating device quality, while also providing insight into underlying physical processes [6]. To date, no scientific reports have been found in the literature on the characterization of graphene/h-BN/Si and hydrogenated graphene/Si junctions through low-frequency noise spectroscopy.

The **aim** of this work is to investigate the low-frequency noise characteristics of graphene-based junctions and graphene field effect transistors with graphene synthesized using the PECVD method. Investigated junctions are with and without h-BN interlayer between graphene and Si substrate, and the other group is hydrogenated graphene/Si junctions. Investigated gFETs are fabricated on a Si/$SiO_2$ substrate.

This Master's thesis is a continuation of the Master‘s scientific research works [7, 8]. Based on a part of the results of this thesis, a publication was prepared:

- J. Glemža, I. Pliaterytė, J. Matukas, R. Gudaitis, A. Vasiliauskas, Š. Jankauskas, Š. Meškinis, Low-Frequency Noise Characteristics of Graphene/h-BN/Si Junctions, Crystals 2025, 15(9), 747; doi:10.3390/cryst15090747.

Most of the results of this work were presented at conferences:

- 68th International Conference for Students of Physics and Natural Sciences Open Readings, May 13th–16th, 2025 Vilnius, Lithuania;
- 46th Lithuanian National Physics Conference, October 8th – 10th 2025, Kaunas, Lithuania;
- 69th International Conference for Students of Physics and Natural Sciences Open Readings, April 27th–30th, 2026 Vilnius, Lithuania.

# 1. Literature Overview

## 1.1. Graphene and graphene-based electronic devices

### 1.1.1. Graphene's properties

Graphene consists of a single layer of $sp^2$ hybridized carbon atoms arranged in a hexagonal lattice. Each carbon atom in graphene has four valence electrons, three of which form in-plane σ-bonds with neighboring atoms, underpinning graphene‘s notably high mechanical strength [9]. The fourth electron occupies a $p_z$ orbital perpendicular to the lattice plane and contributes to a delocalized π electron system. This delocalization gives rise to π and π* energy bands, which largely determine graphene‘s electronic properties. These bands intersect at discrete points in graphene‘s Brillouin zone, called Dirac points, where they form a cone-like shape (Fig. 1). In undoped graphene, the conduction and valence bands meet exactly at the Fermi level (can shift through doping or external bias) [10]. As a result, graphene is a zero-band-gap semiconductor (or semimetal). Near the Dirac points, the energy dispersion relation is linear, resulting in charge carriers behaving like massless Dirac fermions and density of states increasing linearly with energy [9]. In high-quality graphene devices, the Dirac point appears extremely sharp. This sharpness reflects the minimal presence of disorder and charged impurities [11].

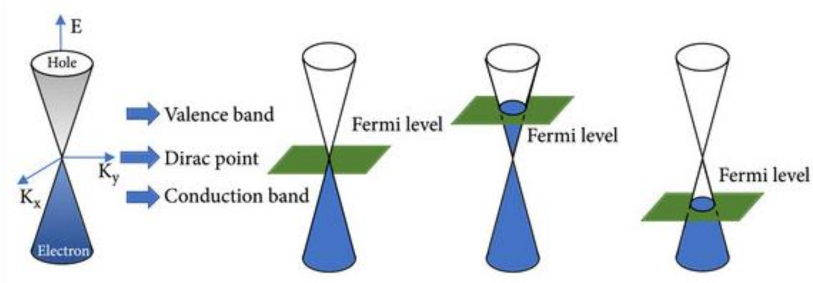


**Fig. 1.** Electronic band structure of graphene and Fermi level variations [10].

Graphene exhibits several exceptional properties that make it highly attractive for electronic and optoelectronic device applications. It has high carrier mobility, reaching $10^4$ $cm^2V^{-1}s^{-1}$ at room temperature and high optical transmittance of 97.7 %. [2]. In addition, it is characterized by excellent thermal conductivity due to strong in-plane σ-bonds and tensile strength ten times that of steel [1].

### 1.1.2. Hydrogenated graphene

Hydrogenated graphene forms when hydrogen atoms covalently bond to carbon atoms in the graphene lattice (Fig. 2). Hydrogenation changes carbon hybridization from $sp^2$ to $sp^3$, and the delocalized π-electron network, responsible for graphene's semimetallic behaviour, is disrupted. In the case of full hydrogenation, graphene is converted into a fully $sp^3$-hybridized structure, also known as graphane [12]. However, experimentally synthesized hydrogenated graphene is typically only partially hydrogenated, resulting in non-uniform hydrogen coverage.

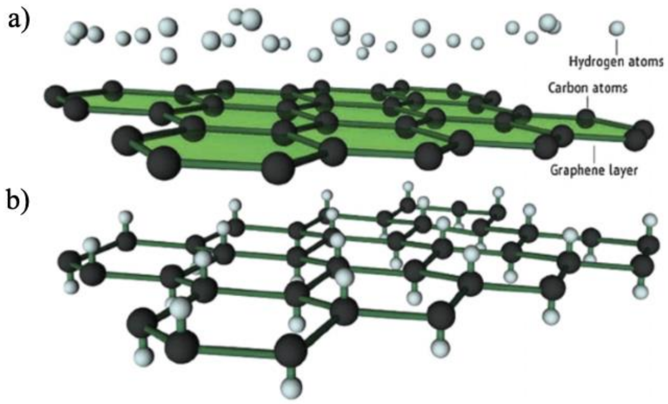


**Fig. 2.** A graphene layer, exposed to a beam of hydrogen atoms (a); hydrogenated graphene layer (b) [13].

One of the key consequence of graphene hydrogenation is that disruption of the $sp^2$ network can lead to bandgap opening. Depending on the degree of hydrogenation, bandgap can range from 0 to 5.4 eV [12]. Thus, hydrogenation can shift graphene's behaviour from semimetallic toward semiconducting or even insulating. This bandgap tunability expands electronic and optoelectronic graphene-based device applications. For example, it has been considered for development of atomically thin transistors [14]. In addition, hydrogenation modifies optical properties of graphene as well, resulting in high transparency in visible-range and photoluminescent behaviour [15]. In particular, hydrogenated graphene has been employed as an interlayer in graphene/Si photodetectors, where improved device performance was attributed to interface passivation and reduction of dark current [16]. Other possible applications of hydrogenated graphene include hydrogen storage [17] and spintronic applications due to observed ferromagnetic properties [18].

### 1.1.3. PECVD growth of graphene

Graphene can be fabricated via several different methods. The highest quality graphene is obtained using mechanical exfoliation, however, only small area graphene flakes can be produced, and it is hard to implement for large-scale industrial applications. Chemical vapor deposition (CVD) is one of the most established methods for large-area graphene synthesis. However, conventional CVD involves film growth on metal catalysts such as Cu or Ni and subsequent transfer procedure onto the target substrate, which is prone to degrading film quality by introducing contamination and structural defects like wrinkles [19]. Therefore, direct graphene growth on the substrate is highly desirable.

During plasma-enhanced chemical vapor deposition (PECVD) reactive species are generated by plasma, which assist precursor gas dissociation, reducing the thermal energy required as compared to conventional CVD. This enables catalyst-free graphene growth directly on semiconductor substrate at significantly lower temperatures [20]. In [3] it was shown that controllable growth of relatively good quality graphene can be achieved via PECVD at 700 °C (Fig. 3). A more recent study has shown that hydrogenated graphene growth can be sustained at even lower temperatures by adjusting PECVD growth parameters [21]. In this study, hydrogenated graphene growth was achieved at temperatures as low as 450 °C – 500 °C by controlling $H_2$ and $CH_4$ gas flow rates, their ratio, and working pressure (Fig. 3).

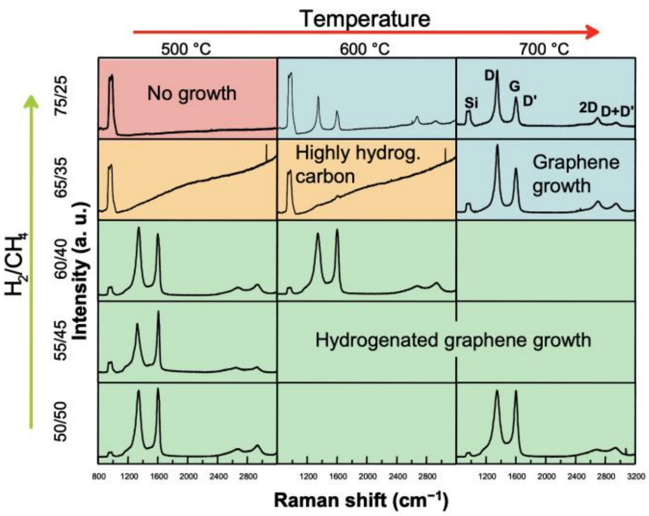


**Fig. 3.** Raman spectra, representing different carbon growth regimes (no growth, highly hydrogenated carbon, hydrogenated graphene and graphene) depending on PECVD synthesis temperature and $H_2/CH_4$ gas flow ratio at 20 mBar work pressure [21].

### 1.1.4. Graphene/Si junctions

The attractive electronic and optical properties of graphene promote the exploration of graphene/semiconductor junctions as alternatives to conventional metal/semiconductor Schottky junctions. Silicon is a natural choice of semiconductor to interface with graphene because it is well understood and very scalable. When graphene and silicon are brought into contact, a Schottky or an ohmic junction can form. In the case of n-type Si, a Schottky junction forms if graphene's work function is sufficiently (typically ~0.4 eV [22]) higher than silicon's Fermi level (Fig. 4). Due to this energy difference, upon contact electrons transfer from Si to graphene and leave positively charged ionized donors, causing a depletion region near the Si surface to form. Charge redistribution causes Si conduction and valence bands to bend upward, and a built-in field is created, which opposes further electron flow from Si to graphene. Assuming the absence of Fermi level pinning, Schottky barrier height is then determined as the difference between graphene work function ($\varphi_{Gra}$ in Fig. 4) and silicon's electron affinity ($\chi$ in Fig. 4) [23]. The effective Schottky barrier height is modulated with applied voltage.

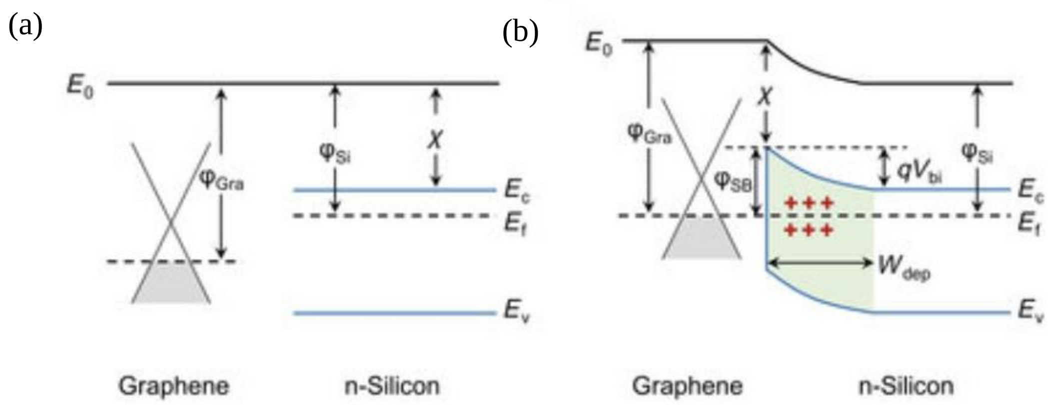


**Fig. 4.** Energy band diagram before (a) and after (b) graphene and n-Si contact; $E_0$ – vacuum level. Adapted from [23].

Graphene/Si junctions are promising for several electronic and optoelectronic device applications. They are extensively explored as solar cells, where graphene's transparency and conductivity can be exploited for efficient charge collection [2]. Since graphene's Fermi level can be tuned by applied bias or by gate voltage, graphene-based Schottky diodes are attractive for application in barristors. Other applications include photodetectors and gas sensors [24].

Despite the potential, graphene/Si junctions still face unresolved issues leading to their limited performance. The main challenge is the large variation of ideality factor, ranging up to ~30 [25]. These deviations are attributed to barrier height inhomogeneities, series resistance or shunt resistance (accounting for leakage current due to trap states and interface defects) [23].

### 1.1.4.1. h-BN as an insulating interlayer for graphene/Si junctions

One of the main issues for graphene/semiconductor junctions is surface recombination, caused by semiconductor dangling bonds (or unsatisfied valence electrons) at the graphene/semiconductor interface, facilitating leakage currents and reduced carrier lifetime, which can severely hinder the performance of photovoltaic devices. The insertion of a thin insulating layer at the graphene/semiconductor interface is widely proposed as a strategy to passivate these unsatisfied bonds [5]. Hexagonal boron nitride (h-BN) is considered as a highly suitable material for this purpose and has been linked to leakage current reduction [26] and improved performance of graphene/Si solar cells [27]. Hexagonal boron nitride (h-BN) is a 2D hexagonal structure material with a very similar lattice parameter to graphene's, which allows to create high quality graphene/h-BN interfaces. It is an insulator with a bandgap of 5.97 eV and, in an ideal case, has no surface dangling bonds. In addition, insertion of an insulating layer of h-BN between graphene and Si increases the effective barrier height of Schottky junction, improving the rectifying behaviour [26].

#### 1.1.4.2. Charge transport in Schottky and MIS junctions

Charge transport in graphene-based semiconductor heterostructures can happen through several different mechanisms. Thermionic emission is widely accepted as a dominant conduction mechanism in graphene/semiconductor junctions. However, real world devices can exhibit multiple conduction regimes depending on device structure, applied bias, temperature, interface properties and defect density [28]. This section will briefly introduce the conduction mechanisms often observed in graphene/Si junctions.

Ohmic conduction is characterized by a linear relationship between current and applied voltage and is due to free-carrier transport through available conductive pathways. Ohmic regime is commonly observed at low bias but may persist over wider voltage ranges.

As the applied voltage changes, transport behaviour may become nonlinear, indicating that injection or barrier controlled conduction mechanisms start to dominate. In an ideal Schottky junction, this behaviour is described by thermionic emission, where carriers with sufficient thermal energy overcome the potential Schottky barrier (Fig. 5 (a)). The current density for thermionic emission for n-type semiconductor is given by [28]:

$$J = J_{\mathrm{s}}\left[\exp\left(\frac{qE}{k_{\mathrm{B}}T}\right) - 1\right], \tag{1}$$

where $J_s$ is saturation current density, expressed as:

$$J_{\mathrm{s}} = A^{*}T^{2}\exp\left(-\frac{q\phi_{\mathrm{SB}}}{k_{\mathrm{B}}T}\right), \tag{2}$$

where $A^{*}$ is the Richardson constant, $q\phi_{\mathrm{SB}}$ is the Schottky barrier height ($\varphi_{\mathrm{SB}} = q\phi_{\mathrm{SB}}$ [eV]), $k_{\mathrm{B}}$ - Boltzmann constant, $T$ – temperature. When an insulating interlayer (e.g. h-BN) is introduced between graphene and semiconductor, a metal-insulator-semiconductor (MIS) type of structure is formed and transport becomes more complex. In this case, not all of the applied voltage contributes directly to semiconductor band bending since carrier transport is also influenced by the dielectric layer. As a result, saturation current density, expressed in Eq. (2), is modified [28]:

$$J_s = A^* T^2 \exp\left[\frac{-q\left(\phi_{\mathrm{SB}} - \sqrt{qE/4\pi\varepsilon_i}\right)}{k_{\mathrm{B}}T}\right], \tag{3}$$

where $\varepsilon_i$ is insulator dynamic permittivity and $E$ is electric field ($E = U/d$, where $d$ is insulator thickness). It is important to note, that in such systems, multiple transport mechanisms can coexist and the dominant mechanism depends on insulating layer thickness, dielectric permittivity, trap density and distribution, as well as operating conditions [28].

Besides thermionic emission, tunneling and Poole-Frenkel emission may contribute (Fig. 5 (b)). In the Poole-Frenkel mechanism, carriers, trapped in dielectric, gain sufficient thermal energy to escape into the conduction band. The resulting current density is given by [28]:

$$J_s \sim E \exp\left[\frac{-q\left(\phi_{\mathrm{SB}} - \sqrt{qE/\pi\varepsilon_i}\right)}{k_{\mathrm{B}}T}\right]. \tag{4}$$

In the case of a thin insulator, direct tunneling current can be also observed in MIS structures (Fig. 5 (c)).

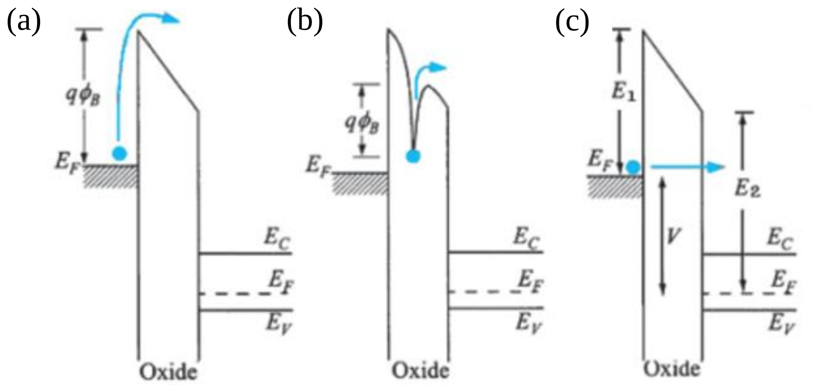


**Fig. 5.** Energy band diagrams and different conduction mechanisms: thermionic emission (a), Poole-Frenkel emission (b), direct tunneling (c) [29].

At higher injection levels, charge transport may transition into the space-charge-limited current (SCLC) regime, which occurs when the density of injected carriers exceeds the intrinsic free carrier density of the material and accumulated charge creates an internal electric field gradient, limiting the current. SCLC is commonly identified from I-V characteristics analysis on a log-log scale, where different slopes ($I \sim U^m$) correspond to distinct transport regimes (Fig. 6) – ohmic conduction (m = 1), trap-limited and trap-free SCLC (m = 2) [30]. Trap-free SCLC is expressed by Mott-Gurney law:

$$J = \frac{9\varepsilon\mu U^2}{8d^3}, \tag{5}$$

where $J$ – current density, $\mu$ – mobility and $d$ – sample thickness [31]. Only regions (1) and (4) appear when the material contains no traps or when carrier transport is not governed by trap states (Fig. 6).

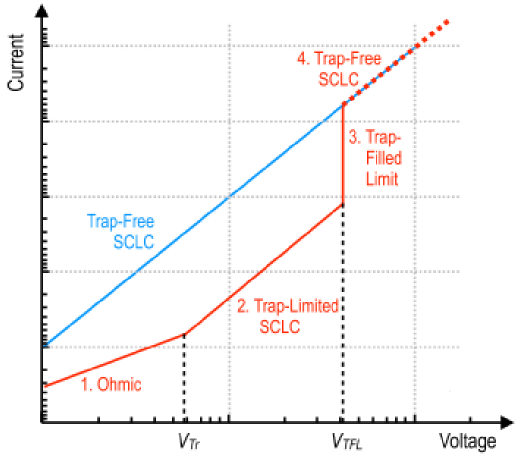


**Fig. 6.** Theoretical I-V curve in log-log scale and typical regimes in the SCLC mechanism. Voltage $V_{Tr}$, denotes the onset of the trap-limited SCLC and trap-filled limit is reached at $V_{TFL}$ [30].

### 1.1.5. Graphene field-effect transistors

A field-effect transistor (FET) is an electronic device in which an electric field, produced by an applied gate voltage, controls the flow of charge carriers through a semiconductor channel. The device typically consists of three terminals: a source and a drain connected by the channel, and a gate electrode that modulates charge transport by varying the magnitude and polarity of the applied voltage. Although the first metal-oxide-semiconductor FET (MOSFET) was successfully fabricated in 1959, there is still a demand for ultra-fast, highly efficient, low-power consumption, and flexible electronics. The conventional Si MOSFET technology faces the short-channel effect when the channel is below 10 nm, since the source and drain regions merge, causing the gate to lose control over the channel. Due to the mentioned attractive graphene properties, the graphene field-effect transistors (GFETs) are promising devices to overcome these issues [32]. GFETs are conventional FET devices in which the channel between the source and drain is formed by a graphene layer. Graphene transistors feature an ambipolar channel, meaning the channel can conduct both electrons and holes depending on the applied gate voltage (Fig. 7), rather than restricting current to a single carrier type as in traditional semiconductors. Graphene transistors are still in the development phase. For example, compared to regular FETs, gFETs cannot be turned off effectively due to the absence of a bandgap. The bandgap of graphene can be tuned by doping, chemical modification, using uniaxial strain, graphene-substrate interaction or breaking the inversion symmetry in bilayer graphene [33]. P-type graphene channel can be easily achieved under air and oxygen atmosphere.

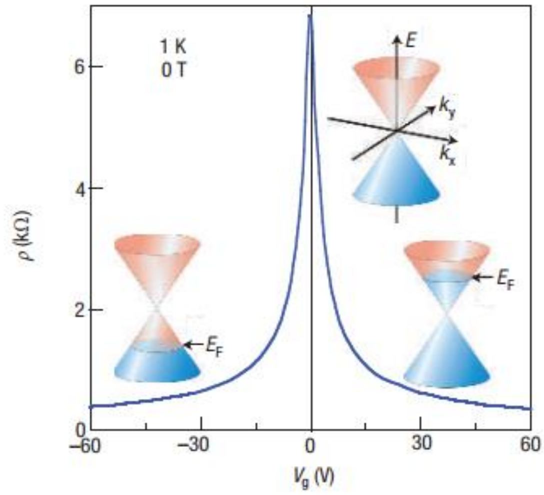


**Fig. 7.** Resistivity vs. gate voltage characteristic showing ambipolar electric field effect in single-layer graphene. The insets show its conical low-energy spectrum $E(k)$, indicating changes in the position of the Fermi energy $E_F$ with changing gate voltage $V_g$ [34].

GFETs have already reached the cut-off frequency record $f_T$ = 427 GHz, close to maximum $f_T$ = 688 GHz, exhibited by well-established III–V material system high-electron mobility transistors (HEMTs) [35].

Due to attractive graphene properties, gFETs are being used in circuits such as high-speed analog circuits-voltage-controlled current sources, radio frequency devices – frequency doubler, frequency tripler, mixer, frequency multiplier, sensors – g-FET-based DNA sensors and gas sensors. Exposing this conductive channel enables the highly sensitive detection of molecules such as hemoglobin, ammonia, glucose, hydrogen peroxide, etc. The electric behavior of gFET can be used to realize the motion of Bio molecules and pH identification [1]. Multiple Dirac points can also be used for creating a logic inverter, e. g. when two graphene transistors with different Dirac voltages are connected in series [36].

The gFET with high mobility values can outperform regular FETs, however since mobility of carriers varies depending on the semiconductor material used, identifying material that gives high mobility is an open problem [1]. Mobilities of 147 $cm^2V^{-1}s^{-1}$ and 707 $cm^2V^{-1}s^{-1}$ were reported for directly grown graphene FETs with channel sizes of 20 × 30 µm and 10 µm × 10 µm, respectively. CVD graphene transferred onto the $SiO_2$ typically shows higher mobilities, e.g. ~1350 $cm^2V^{-1}s^{-1}$, although values as low as 89 $cm^2V^{-1}s^{-1}$ have also been reported [4].

## 1.2. Low-frequency noise and it's classification

Electronic noise is defined as random fluctuations of microscopic quantities, such as voltage or current, around their average values. Various microscopic processes, including thermal agitation of carriers or temporal instabilities in device parameters might lead to these fluctuations [37]. Depending on physical origin or spectral form, low-frequency noise is classified into several different types, which are briefly introduced in the following subsections.

### 1.2.1. Thermal noise

Thermal noise is an intrinsic noise present in all resistive elements at non-zero temperatures as it is rooted in the random thermal motion of charge carriers. Because of its thermal origin, this type of noise exists even in passive components without any applied bias. Thermal noise is considered white noise, since its spectral density is flat up to very high frequencies (on the order of $10^{12}$ Hz) due to very short charge carrier relaxation time. For a resistor of resistance $R$ at temperature $T$, the voltage noise spectral density is given by [37]:

$$S_U(f) = 4k_B TR, \tag{6}$$

where $k_B$ is Boltzmann's constant. Because the spectral density of thermal noise is fully determined by resistance and temperature, resistors with known resistances are commonly used to calibrate noise measurement systems [6]. Being fundamentally unavoidable, thermal noise also defines the lowest fluctuation level below which other noise components cannot be detected.

### 1.2.2. Shot noise

Shot noise is another type of white noise, caused by discrete nature of charge carriers, and manifests due to their random emission through a potential barrier. The current spectral density $S_I$ of shot noise is described by [6]:

$$S_I = 2qI, \tag{7}$$

where $q$ is elementary charge and $I$ is current.

### 1.2.3. RTS and generation-recombination noise

Capture and emission from trap centers cause local modifications of conductance, which results in random telegraph signals (RTS). A signal originating from a single individual fluctuator (trap center) with characteristic mean capture and emission times $\langle\tau_0\rangle$ and $\langle\tau_1\rangle$ produces a Lorentzian shaped power spectral density:

$$S_I(f) = \frac{4(\Delta I)^2}{(\langle\tau_0\rangle + \langle\tau_1\rangle)[(1/\tau_{\text{eff}})^2 + (2\pi f)^2]}, \tag{8}$$

where $\tau_{\text{eff}}$ is effective time, related to $\langle\tau_0\rangle$ and $\langle\tau_1\rangle$ by:

$$\frac{1}{\tau_{\text{eff}}} = \frac{1}{\langle\tau_0\rangle} + \frac{1}{\langle\tau_1\rangle}. \tag{9}$$

RTS noise and generation-recombination (g-r) noise are fundamentally the same physical phenomenon – charge carriers being captured and emitted by a localized defect level. However, they are distinguished by the scale of the device and the number of active traps involved. RTS noise is essentially the single-trap (or a few traps) limit of g-r noise and dominates in nanoscale or sub-micron semiconductor devices and usually affects the conduction only locally [38].

### 1.2.4. 1/*f* noise

1/*f* noise (or flicker noise) is characterized by a power spectral density that scales inversely with frequency as $\sim 1/f^\gamma$, where $\gamma$ is close to unity [37]. This spectral behaviour is explained by a superposition of contributions of many individual fluctuators, described by Eq. (8), with a wide distribution of characteristic time constants [38]:

$$S_U(f) \propto I^2 \sum_{k=1}^{K} \frac{(\Delta R_k)^2}{(\langle\tau_0\rangle + \langle\tau_1\rangle)_k[(1/\tau_{\text{eff}})_k^2 + (2\pi f)^2]}, \tag{10}$$

where $k = 1, 2, \ldots, K$ and $K$ is the number of traps in a device.

An empirical formula, used to estimate the noise level, was proposed by H. N. Hooge [37]:

$$\frac{S_R}{R^2} = \frac{S_U}{U^2} = \frac{S_I}{I^2} = \frac{S_U}{U^2} = \frac{\alpha}{Nf}, \tag{11}$$

where $N$ is the number of free carriers in the sample and $\alpha$ is a dimensionless parameter, used to characterize the 1/*f* noise intensity.

## 1.3. Low-frequency noise and defects in graphene and graphene-based devices

Graphene is often idealized as a perfect two-dimensional lattice, but in practical realizations some extent of defectiveness in graphene is inevitable [39]. This is especially true for graphene synthesized by chemical vapor deposition (CVD) techniques, where the polycrystalline nature of the films unavoidably leads to the formation of grain boundaries [40, 41]. Grain boundaries are intrinsic line defects that form when domains with different crystal orientations nucleate and merge. The synthesis method used for the samples investigated in this work – PECVD – has been linked to an even higher density of defects than conventional CVD. A pronounced D peak in the Raman spectrum of PECVD-grown graphene has been consistently observed, indicating structural disorder of the graphene lattice [3].

Apart from grain boundaries, other defects can be present in graphene in the context of PECVD growth. These include foreign atoms and vacancies. Foreign atoms are extrinsic defects and can be adsorbed onto the graphene lattice as adatoms, a prevalent example being hydrogen adatoms. Foreign atoms can also replace carbon atoms in graphene's lattice. Boron and nitrogen are regarded as natural dopants in graphene because of their comparable atomic radii to carbon, but differing numbers of valence electrons. Vacancies or missing atoms are possible intrinsic point defects and can form in the high-energy plasma environment, despite the fact that simultaneously high temperatures cause annealing, reducing them [39].

Defects in graphene have a strong impact on its electronic performance and charge transport. They act as scattering centers for charge carriers, influencing carrier mobility and electrical conductivity, and can also alter electronic band structure around defect sites, causing localized electronic states or modifications in doping level [39, 40]. Subsequently, structural defects in graphene correspond to increased low-frequency noise levels [41, 42].

Several notable properties of 1/*f* fluctuations in graphene have already been reported in the scientific literature. Although the first reports of 1/*f* noise in graphene appeared in 2008, it still lacks a uniform theory explaining the microscopic mechanism of the conductivity fluctuations in graphene-based devices. Usually, the carrier-number-fluctuation or mobility-fluctuation mechanisms of 1/*f* noise are distinguished [42]. In particular, bilayer graphene in FET structure has been shown to exhibit substantially lower 1/*f* noise levels compared to monolayer graphene, owing to the more effective screening of potential fluctuations induced by external impurity charges [43]. Observed electrical noise dependences on gate voltage are also different compared to the usual characteristics of field effect transistors [42] (will be discussed in Section 3.2.3). The noise in CVD graphene has been found to be at least one order of magnitude larger than in exfoliated graphene [42]. A significant contribution of contact noise in gFETs has also been identified. The current crowding effect has been demonstrated to play a significant role at graphene–metal junctions as well [44]. It should be noted that, in most cases, when the graphene/Si photodetectors are investigated, usually only noise equivalent power (NEP) and dark current noise are estimated or calculated [45, 46], regardless of the existence of flicker noise. Only a few papers have investigated the low-frequency noise characteristics of graphene/Si junctions in detail [25, 47]. However, there remains a lack of scientific research on the low-frequency noise characteristics of hydrogenated graphene and junctions based on it, as well as on graphene junctions with an inserted h-BN interlayer. No scientific articles were found that investigated the noise characteristics of gFETs in which graphene was synthesized using the PECVD method.

# 2. Experiment

## 2.1. Investigated samples

### 2.1.1. Graphene/Si junctions

Graphene/Si junctions with different configurations were investigated – structures with an inserted h-BN interlayer and junctions with hydrogenated graphene on Si. Structures of the investigated devices are shown in Fig. 8. Comparison with the reference graphene/Si junction without the h-BN interlayer has also been performed.

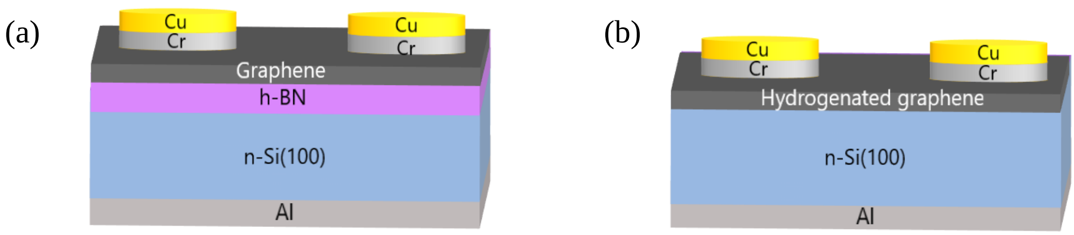


**Fig. 8.** Structures of the investigated devices: graphene/h-BN/n-Si(100) (a) and hydrogenated graphene/n-Si(100) (b).

All investigated graphene/Si junctions were fabricated on n-type Si(100) wafers, manufactured by Sil'tronic Silicon Technologies, as a substrate. For samples with an h-BN interlayer, h-BN films were first deposited on the substrate by high-power impulse magnetron sputtering (HIPIMS). Junctions with h-BN layer thicknesses of 1, 3, 5, and 15 nm were investigated.

Graphene was directly synthesized on the substrates using microwave plasma-enhanced chemical vapor deposition (PECVD). Hydrogenated graphene samples were grown at a reduced temperature of 500 °C, compared to typical temperatures of 700 °C or higher required for pristine graphene growth [21]. To sustain growth at the lower temperature, a higher working pressure of 20 mBar was used instead of 10 mBar for growth at 700 °C. Hydrogen and methane gas flow rates (in standard cubic centimeters per minute, sccm), and thus the $H_2/CH_4$ flow ratios, were varied across the hydrogenated graphene sample groups. The synthesis conditions are summarized in Table 1. An Al film was deposited by e-beam evaporation to form a common contact, and the Cr/Cu electrodes were vacuum evaporated on the graphene via a mask with 500 µm circular holes.

**Table 1.** PECVD synthesis parameters of graphene for the investigated graphene/Si junctions.

| Junctions | Sample group No | Synthesis temperature (°C) | $H_2$ flow (sccm) | $CH_4$ flow (sccm) | Pressure (mBar) | $H_2/CH_4$ flow ratio |
|---|---|---|---|---|---|---|
| Hydrogenated graphene/n-Si junctions | 1 | 500 | 80 | 70 | 20 | 1.14 |
| | 2 | 500 | 110 | 90 | 20 | 1.22 |
| | 3 | 500 | 120 | 80 | 20 | 1.5 |
| Graphene/h-BN/n-Si(100) junctions | | 700 | 75 | 25 | 10 | |

## 2.1.2. Graphene field-effect transistors

A further set of samples, investigated in this work, consists of graphene field-effect transistors. Silicon substrates coated with a 300 nm $SiO_2$ layer, formed by thermal oxidation of single-crystal Si(100) wafers (Sil'tronix, Archamps, France), were used. Graphene was synthesized using the microwave PECVD system, as in the case of the investigated junctions. Graphene synthesis parameters are shown in Table 2.

**Table 2.** PECVD graphene synthesis parameters of the investigated gFETs.

| No | Synthesis temperature (°C) | $H_2$ flow (sccm) | $CH_4$ flow (sccm) | Pressure (mBar) |
|---|---|---|---|---|
| **762** | 700 | 75 | 25 | 20 |
| **769** | 700 | 75 | 25 | 10 |
| **770** | 650 | 75 | 25 | 10 |
| **771** | 750 | 75 | 25 | 10 |
| **772** | 800 | 75 | 25 | 10 |

To form the source and drain contacts, Cr/Cu bilayer electrodes were deposited on graphene by thermal evaporation. Dimensions of each contact were 1.6 mm × 0.4 mm, and the distance between the contacts was 0.4 mm (Fig. 9). A back-gate contact was formed by chemically etching the $SiO_2$ from the back of the sample to expose the Si surface, followed by deposition of an Al film by e-beam evaporation.

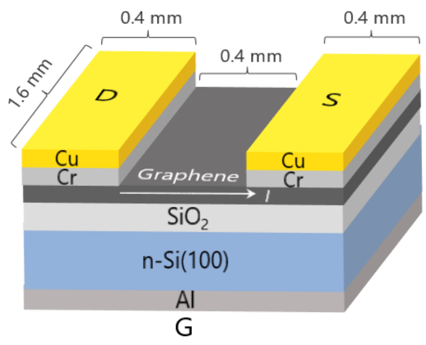


**Fig. 9.** Structure of the investigated gFET.

Raman spectra measurements were performed by the manufacturer (Vacuum and Plasma Processes Research Laboratory, Institute of Materials Science, Kaunas University of Technology). The D peak and G peak intensity ratio $I$(D)/$I$(G) is used to estimate the defect density within the graphene structure, where an increased ratio represents a higher defect density [48]. The D to D′ peak intensity ratio $I$(D)/$I$(D′) is used to identify the dominant graphene defect types. The $I$(D)/$I$(D′) value of ~ 3.5 is linked to grain boundaries, while ~ 1.3 is typical for on-site defects [49]. The 2D peak and G peak intensity ratio $I$(2D)/$I$(G) was employed to appraise the number of layers [50]. A reduction in this ratio implies an increase in the number of graphene layers.

## 2.2. Measurement setup and methods

### 2.2.1. Noise measurement of graphene/Si junctions

Low-frequency noise characteristics of the samples were measured in the 10 Hz – 60 kHz frequency range under both forward and reverse bias. The noise measurements of the graphene/Si junctions were carried out in a shielded laboratory to minimize the influence of external electromagnetic interference. The noise measurement experimental setup is shown in Fig. 10. The device under test (DUT) was biased using a DC power source. The current flowing through the device was adjusted using a potentiometer and monitored using an ammeter, while the voltage across the junction was measured with a voltmeter. To ensure operation under constant current conditions, the load resistor $R_{load}$ was selected to have at least ten times higher resistance than the differential resistance of the DUT. Voltage fluctuations across the DUT were amplified using a low-noise amplifier (LNA). The signal was then passed through a filter (F) and digitized using a sound card (for frequency range in the 10 Hz – 22 kHz) or a National Instruments PCI-6115 analog-to-digital converter (for frequency range in 22 kHz – 60 kHz) (ADC), connected to a PC for analysis. Spectral density of the voltage noise was evaluated using a Fast Fourier Transform (FFT).

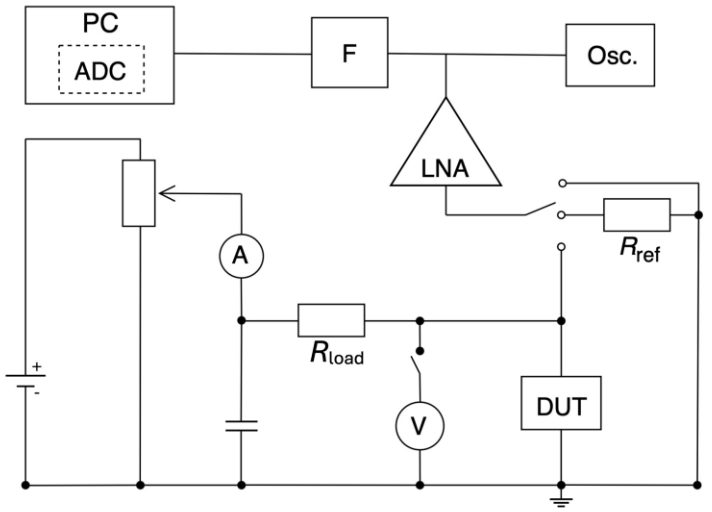


**Fig. 10.** Noise measurement setup schematic: DUT – device under test, $R_{ref}$ – reference resistor, $R_{load}$ – load resistor, LNA – low-noise amplifier, F – filter, ADC – analog-to-digital converter, PC – personal computer, Osc. – oscilloscope.

To find the absolute noise voltage spectral density, the system was calibrated using a known resistor $R_{ref}$. The noise of the DUT was compared to the thermal noise of a known resistor $R_{ref}$ and also taking into account the measurement system noise using a three-step measurement method. The three steps included measuring voltage noise spectral densities of the DUT, $R_{ref}$ and the measurement system, respectively $S_{DUT}$, $S_{ref}$ and $S_{syst}$, separately and the absolute voltage noise spectral density was calculated using the following formula:

$$S_U = 4k_B T R_{\mathrm{ref}} \frac{S_{\mathrm{DUT}} - S_{\mathrm{syst}}}{S_{\mathrm{ref}} - S_{\mathrm{syst}}}, \tag{12}$$

where $T$ is the absolute temperature of $R_{ref}$.

The I-V characteristics of the investigated devices were measured with the semiconductor device parameter analyzer Agilent B1500A. For temperature-dependent measurements below room temperature, the samples were cooled with liquid nitrogen. For measurements above room temperature, a Peltier element was used. To monitor the temperature during measurements, a Pt100 platinum resistance temperature sensor was used [7, 8].

### 2.2.2. Noise measurement of graphene field-effect transistors

The low-frequency noise measurement setup for graphene samples in FET configuration is represented in Figure 11. All graphene field-effect transistors' noise and transfer characteristics (drain current ($I_{ds}$) vs. gate voltage ($U_g$)) measurements have been performed in the following sequence at room temperature. Firstly, a positive gate voltage was varied from zero to +62 V for the constant drain-source voltage $U_{ds}$ = 0.2 V. Then, a negative voltage was varied starting from zero and ending at -62 V for the same voltage $U_{ds}$ = 0.2 V. This $U_{ds}$ value was selected as it represents a significant point for chemical sensing mechanisms in gFETs with pristine and defective graphene layers and is often selected for data analysis in scientific papers [4]. In [51], it was demonstrated that defective graphene and carbon nanotube (CNT) sensors are insensitive to gas adsorption at low applied voltages until a critical potential is reached. While for pristine graphene FETs, it was determined that within a low Uds range (up to 200 mV), there is no effect of the applied $U_{ds}$ on the absorption/desorption of trace gas vapor molecules, and the sensitivity decreases above this voltage [52]. During each measurement, the load resistance was carefully adjusted using the potentiometer to set the desired voltage $U_{ds}$ = 0.2 V. Electrical fluctuations were amplified by a low-noise amplifier and absolute voltage spectral densities were calculated by comparing noise of the DUT to the reference resistor thermal noise, i.e. the procedure is the same as for graphene/Si junctions (Eq. (12)).

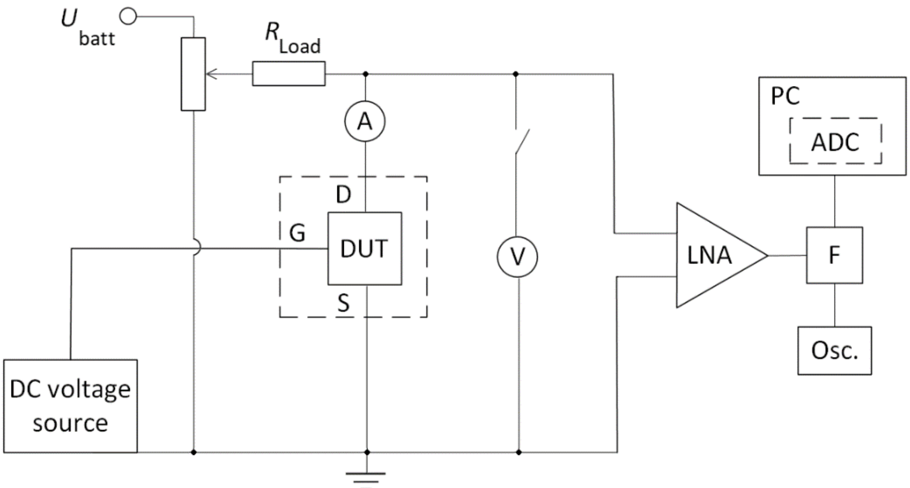


**Fig. 11.** Low-frequency noise measuring system. A – ammeter, DUT – device under test, D – drain, G – gate, S – Source, LNA – low-noise amplifier, F – filter, ADC – analog digital converter, V – voltmeter, $R_{load}$ – load resistance, $U_{batt}$ – battery, Osc. – oscilloscope, PC – personal computer.

# 3. Results and discussion

## 3.1. Investigation of graphene/Si junctions

### 3.1.1. Current-voltage characteristics of graphene/Si junctions

I-V characteristics of the graphene/Si junctions under both forward and reverse bias were measured. Typical characteristics of samples with different h-BN layer thicknesses at room temperature are shown in Fig. 12. At forward bias in the low voltage regime the current scales linearly with voltage, indicating dominant ohmic conduction behaviour (Fig. 12 (a)). At higher forward voltages, a clear nonlinearity appears for all samples, indicating possible Schottky emission or other field-enhanced conduction mechanisms like Poole-Frenkel emission or tunneling. In graphene/semiconductor junctions Schottky emission is widely accepted as a dominant conduction mechanism [22]. However, when an insulator is inserted between graphene and semiconductor, the determination of current conduction requires special attention. For example, the Richardson coefficient in Schottky equation should be modified with a transmission coefficient that depends on the barrier height between the semiconductor and the insulator [28]. No major differences are observed between samples I-V with and without h-BN interlayer.

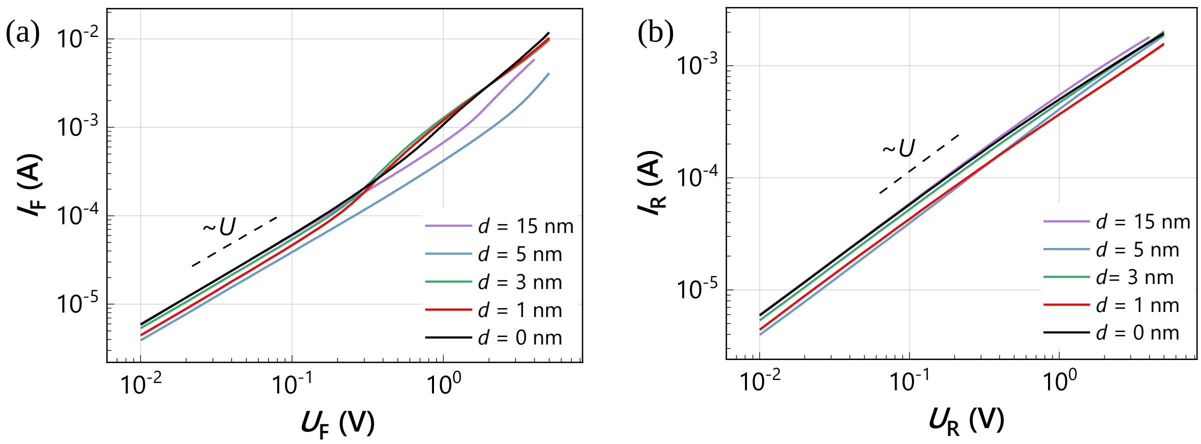


**Fig. 12.** Typical forward (a) and reverse (b) I-V characteristics of investigated graphene/h-BN/Si junctions with different h-BN layer thicknesses at room temperature; *d* – h-BN interlayer thickness.

Larger differences were observed across the investigated hydrogenated graphene/Si junctions. Fig. 13 shows representative I-V curves from each of the investigated groups, corresponding to different $H_2/CH_4$ flow ratios. At forward bias in the low voltage regime, current scales linearly with voltage, indicating dominant ohmic conduction. At higher forward bias, the I-V curves show significant differences depending on the $H_2/CH_4$ flow ratios used during graphene synthesis. The lowest ratio ($H_2/CH_4$ = 80/70) samples (Fig. 13 (a)) exhibit the closest to exponential forward bias I-V characteristic, which can be described by the Schottky equation (Eq. (1)). Samples synthesized with higher $H_2/CH_4$ flow ratios show deviations from Schottky behaviour. For instance, at $H_2/CH_4$ = 110/90, the I-V characteristic becomes step-like (Fig. 13 (b)). The I-V curves are nearly linear across the entire measured range in reverse bias for both groups of investigated junctions (Fig. 13 (b) and Fig. 12 (b)).

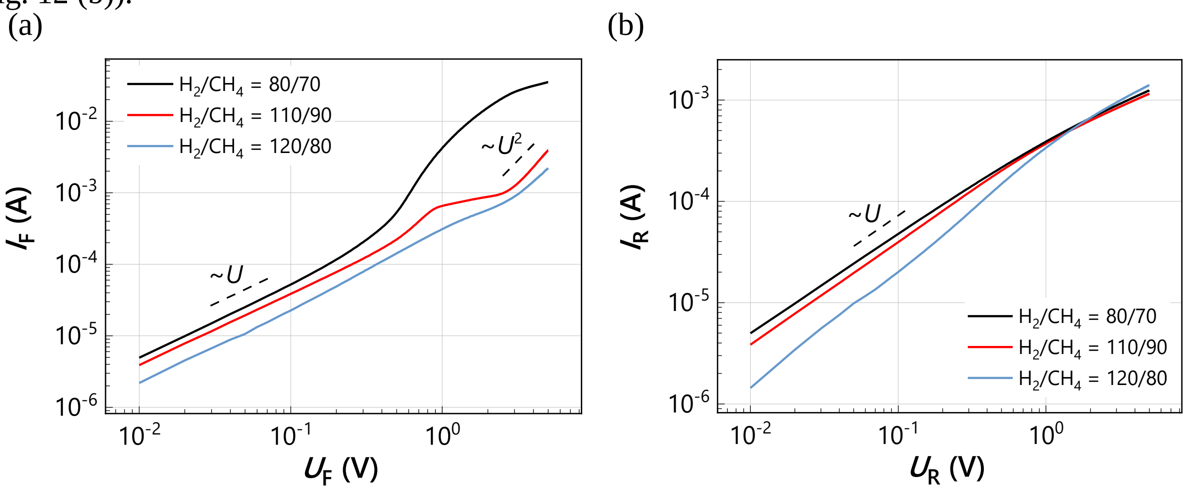


**Fig. 13.** Representative forward (a) and reverse (b) bias I-V characteristics corresponding to different $H_2/CH_4$ flow ratios used during graphene synthesis (sample groups 1-3) at room temperature.

Dominant conduction mechanisms in the investigated junctions is discussed in more detail in Appendix.

### 3.1.2. Electrical noise spectra of graphene/Si junctions

All investigated junctions are mainly characterized by $1/f$ or $1/f^{\alpha}$ – type electrical fluctuations at forward and reverse bias that can be described as a superposition of many Lorentzian-type spectral components due to individual fluctuators with widely distributed characteristic times as described by Eq. (8). In some cases, a particular trap center (or many traps with the same characteristic time constant) contributes significantly more to overall noise than others, making its characteristic Lorentzian spectral shape distinguishable from the $1/f$-type noise background. Such clear Lorentzian-type spectra are observed at particular current and temperature values, where the Fermi energy level coincides with the energy of the defect capture center.

Noise spectra of the representative graphene/h-BN/Si and reference samples at forward bias are shown in Fig. 14. Some investigated junctions with h-BN interlayer are distinguished by the appearance of distinct Lorentzian spectrum at forward bias as in the example of 5 nm h-BN layer sample at 0.1 mA (Fig. 14). In general, only a few Lorentzian-type noise spectra are observed.

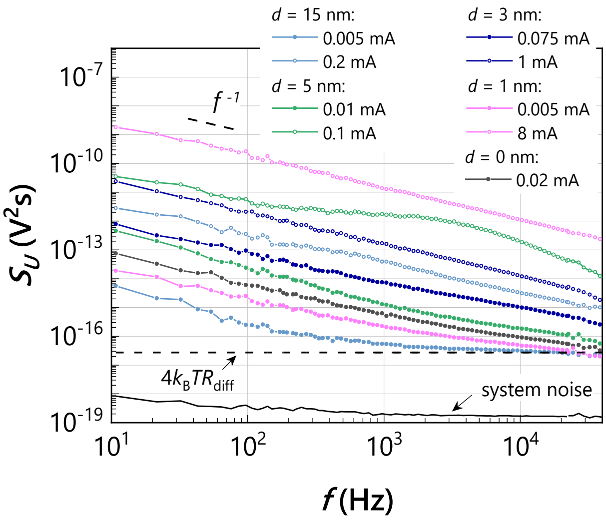


**Fig. 14.** Representative noise spectra, measured at forward bias at room temperature for graphene/h-BN/Si junctions with different h-BN layer thicknesses; *d* – h-BN interlayer thickness.

Significantly larger differences in the noise spectra are observed in hydrogenated graphene/Si junctions. Sample group 1 ($H_2/CH_4$ = 80/70) is characterized by 1/*f* -type fluctuations across the entire investigated forward current range (Fig. 15 (a)). For sample group 2 ($H_2/CH_4$ = 110/90), the spectra are typically 1/*f*-type at the lowest forward currents while a Lorentzian-type spectral component, characteristic of generation-recombination (g-r) noise, emerges at intermediate to high currents (Fig. 15 (b)). For sample group 3, corresponding to the highest $H_2/CH_4$ flow ratio ($H_2/CH_4$ = 120/80), Lorentzian-type (g-r) spectra are observed throughout the entire investigated forward-bias current range (Fig. 15 (c)).

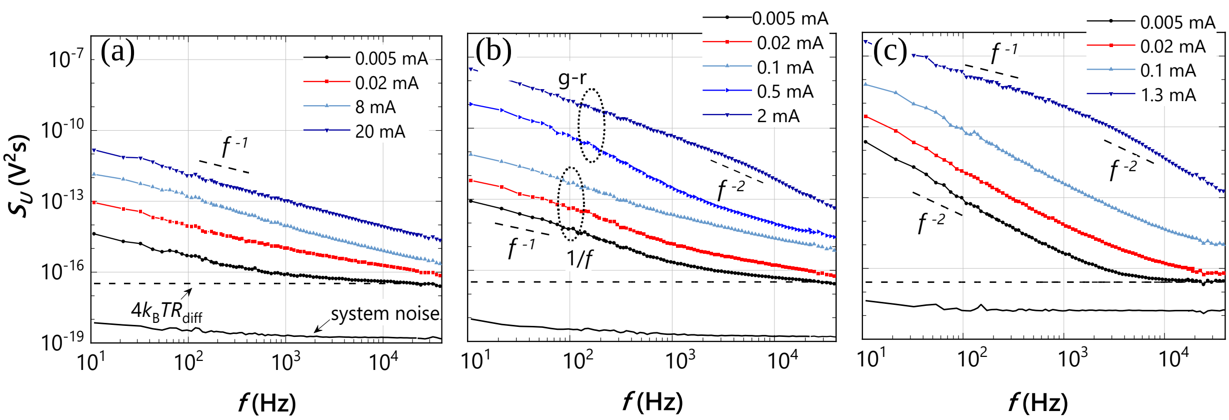


**Fig. 15.** Representative noise spectra, measured at forward bias at room temperature, for junctions with graphene, synthesized using different $H_2/CH_4$ flow ratios: $H_2/CH_4$ = 80/70 (sample group 1) (a), $H_2/CH_4$ = 110/90 (sample group 2) (b), $H_2/CH_4$ = 120/80 (sample group 3) (c).

A white spectral region attributed to thermal noise is observed at low bias, as can be seen in Fig. 14 and Fig. 15. At such low currents, thermal noise is dominant over shot noise and set a limit for the minimum observable noise level. The intensity of thermal noise is determined by the differential resistance of the investigated junction at linear I-V characteristic part. Noise spectra of the investigated junctions at reverse bias are represented in Appendix (Fig. A1).

To investigate the origin of the pronounced Lorentzian spectra observed in several hydrogenated graphene/Si junctions temperature-dependent noise spectroscopy was performed. A representative normalized voltage noise spectra for a group 2 ($H_2/CH_4$ = 110/90) sample in the 295.5 K – 346.6 K temperature range is shown in Fig. 16 (a).

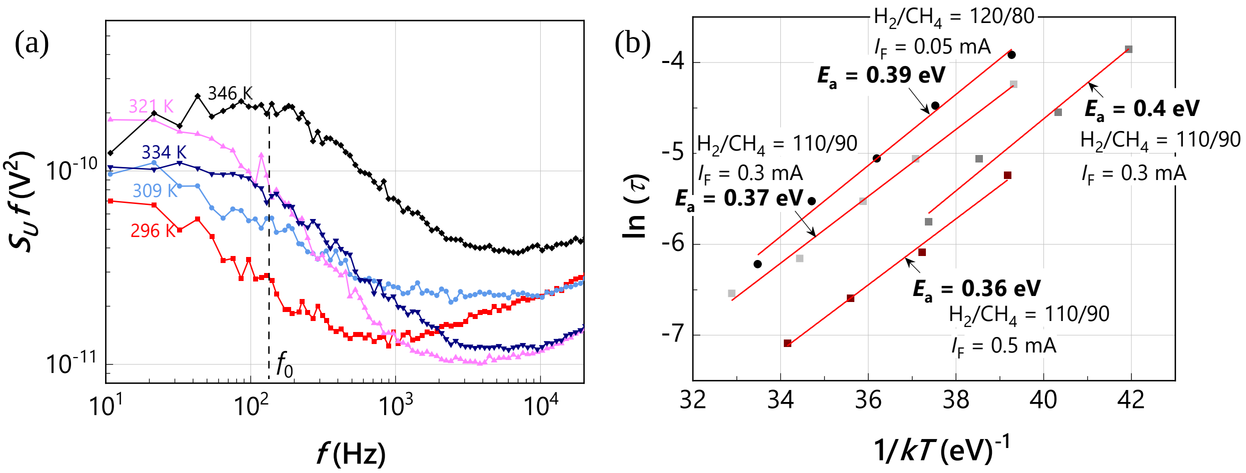


**Fig. 16.** Normalized voltage noise spectral density at different temperatures at forward-bias current of $I$ = 0.05 mA of a group 2 sample ($H_2/CH_4$ = 110/90) (a), where $f_0$ – characteristic corner frequency, and dependences of of the relaxation time on the inverse temperature for samples from different sample groups (b). Experimental conditions and activation energies are presented near the curves. Red lines depict the linear fits.

The characteristic time constants of the Lorentzian components were determined from the corner frequencies $f_0$ (Fig. 16 (a)) as $\tau = 1/2\pi f_0$ and exhibited thermally activated behaviour. Therefore, activation energies were determined by fitting the $\ln(\tau)$ vs. $1/kT$ dependences (Fig. 16 (b)) according to the Arrhenius equation:

$$\tau = \tau_0 \exp\left(\frac{E_a}{k_B T}\right), \tag{13}$$

where $k_B$ - Boltzmann constant, $T$ – temperature [38]. Activation energies ranging from 0.36 eV to 0.4 eV were obtained for samples from groups 2 and 3. Similar activation energies close to 0.4 eV have been reported in literature, where theoretical calculations were performed, where they have been associated with hydrogen or hydroxyl related defects in graphene-based devices near graphene/semiconductor or graphene/oxide interfaces [53], suggesting that such defects may be responsible for the observed g-r behaviour [8].

### 3.1.3. Electrical noise dependence on current of graphene/Si junctions

Both electrical voltage ($S_U$) or current ($S_I$) fluctuation dependencies on current provide valuable information about the physical processes occurring at the junction and the possible dominant conduction mechanisms. In some cases, it is convenient to convert electrical voltage noise to current noise, using the differential resistance $S_I = S_U/R_{\text{diff}}^2$, for example to compare it with the results in the scientific literature or to notice differences between similar voltage noise characteristics.

All of the investigated samples exhibited $S_I \sim I^\gamma$ (or $S_U \sim I^\gamma$) relationship with $\gamma \approx 2$. This dependence was prominent for all of the samples with and without the h-BN interlayer at least at low bias (Fig. 17), where the I-V characteristic is linear. The quadratic dependence of $1/f$ noise intensity on current is typically expected for ohmic samples and is a consequence of intrinsic resistance fluctuations, described by Eq. (11). A deviation from the quadratic dependence at high forward bias, where $S_I$ scales with current with $\gamma > 2$ is observed (Fig. 17 (a)). This noise behaviour can no longer be explained by the conventional resistance fluctuations model (Eq. (11)). The current intervals, where this sharp increase in noise spectral density occurs, also coincide with the non-linear regions of the I-V characteristics (Fig. 12 (a)). Such strong noise dependences on current with $\gamma > 2$ were earlier observed in polycrystalline films [54], where the influence of grain boundaries on the noise characteristics was demonstrated. In investigated junctions, the surface of the h-BN layer, deposited by HIPIMS, is grainy and rougher compared to exfoliated high-crystallinity h-BN flakes. This further enhances the roughness of the graphene grown on the h-BN layer leading to grain boundaries being dominant defects in the investigated devices. Thus, $S_I \sim I^\gamma$, where $\gamma > 2$, can be attributed to grain boundaries, that locally distort current distribution and electric field, and act as a strong noise source [37, 41, 42]. In addition, traps and various impurities near grain boundaries can contribute to the leakage channel formation in the junction and current crowding, which further increases the level of $1/f$ noise [41, 42].

However, reference sample without an h-BN layer is distinguished by different electrical noise vs. forward current characteristic (inset in Fig. 17 (a)). An interval, in which $S_I$ scales approximately linearly with current ($\gamma \approx 1$) is detected within the current range of 0.05 mA to 0.4 mA. The proportionality $S_I \sim I$ is usually attributed to pure thermionic emission in Schottky diodes [25]. Since the $S_U$ dependence on current (Fig. 17 (b)) does not provide such information, it is beneficial to recalculate and investigate current noise dependence. Such a dependence was not observed in samples with a h-BN layer, meaning that a different prevailing conduction mechanism or several mechanisms are contributing. At high currents, the rapid increase in noise intensity shows that not only grain boundaries in h-BN interlayer have a strong influence, but also grain boundaries in graphene play a significant role in the device conduction.

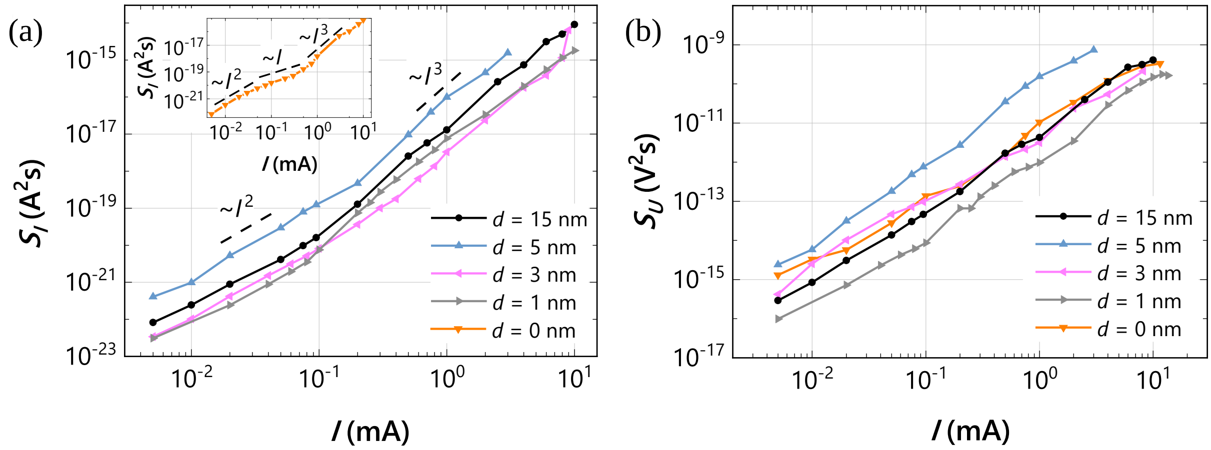


**Fig. 17.** Current (a) and voltage (b) noise spectral density dependencies on current at $f$ = 108 Hz at forward bias; $d$ – h-BN interlayer thickness.

In the case of hydrogenated graphene/Si junctions, noise vs. current characteristics are quite different compared to samples with h-BN interlayers and those found in the scientific literature for Schottky junctions (Fig. 18). In all sample groups, these dependences typically showed a "bump" in the low-current region, followed by a sharp increase in noise intensity at high currents. Due to such an interesting characteristic shape, voltage fluctuations are being considered. To better understand and explain the bump-like behaviour in noise spectral density dependence on current, which is most distinctly visible in the group 1 sample ($H_2/CH_4$ =80/70), a model based on an equivalent electrical circuit is proposed for this sample.

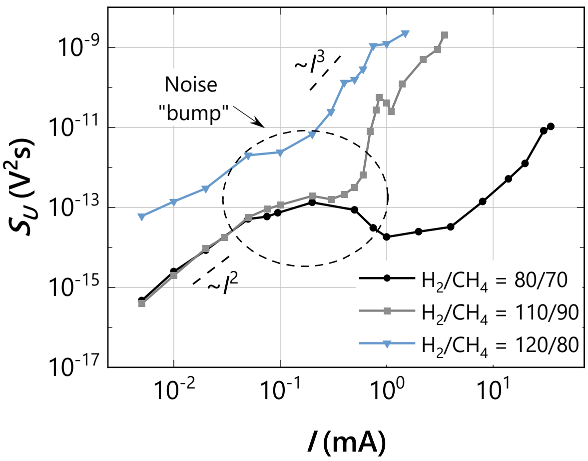


**Fig. 18.** Representative voltage noise spectral density dependencies on forward-bias current for junctions with graphene, synthesized using different $H_2/CH_4$ flow ratios at 108 Hz.

To describe the experimentally measured I-V characteristic (Fig. 19 (a) in black dots), an equation combining Schottky together with the ohmic contribution was used:

$$I = I_0\left(\exp\left[\frac{q(U - IR_s)}{(nkT)}\right] - 1\right) + mU, \tag{14}$$

where $I_0$ – saturation current, $R_s$ – series resistance, $n$ – non-ideality factor of the junction. The term $mU$ represents the low bias ohmic contribution ($m$ – a coefficient). The experimental I-V characteristic was best reproduced using a saturation current $I_0$ of $3 \cdot 10^{-9}$ A, while the ideality factor $n$ was varied between 1.7 and 2.8 within the (0.5 – 1) V bias range. The influence of the series resistance $R_s$ becomes significant at higher bias (above 1 V). The calculated I-V curve is presented in Fig. 19 (a) as a red curve, while the blue curve shows the Schottky contribution excluding the ohmic term.

An equivalent electrical circuit was proposed (Fig. 19 (b)). In this circuit, the investigated junction is represented by the differential resistance $R_d$ ($R_d = dU/dI$), connected in parallel with ohmic resistance $R_p$ ($R_p \approx 2018\ \Omega$) and in series with the resistance $R_s$. Two independent voltage noise sources $u_{R_{p\,1/f}}$ and $u_{R_{s\,1/f}}$, associated with parallel ohmic resistance $R_p$ and series resistance $R_s$, were included to account for the dominant noise contributions.

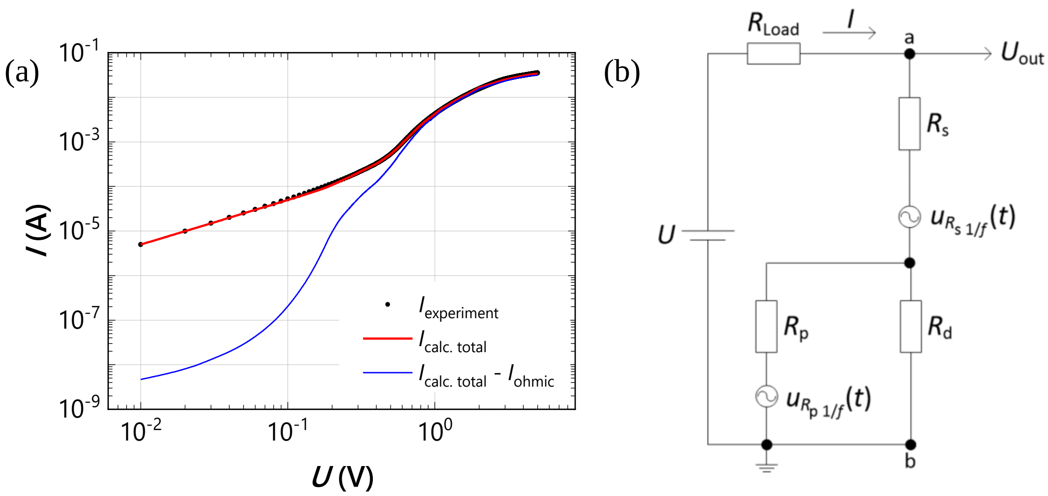


**Fig. 19.** Experimental (black dots), calculated (red curve) forward-bias I-V characteristics of the investigated junction ($H_2/CH_4$ = 80/70) and calculated I-V characteristics excluding the ohmic contribution (blue curve) (a), and equivalent electrical circuit with two noise sources($R_{Load} >> R_{ab}$) (b).

To explain the observed voltage noise dependence shown in Fig. 20 (a), calculated differential and ohmic resistance dependences on current are presented in Fig. 20 (b).

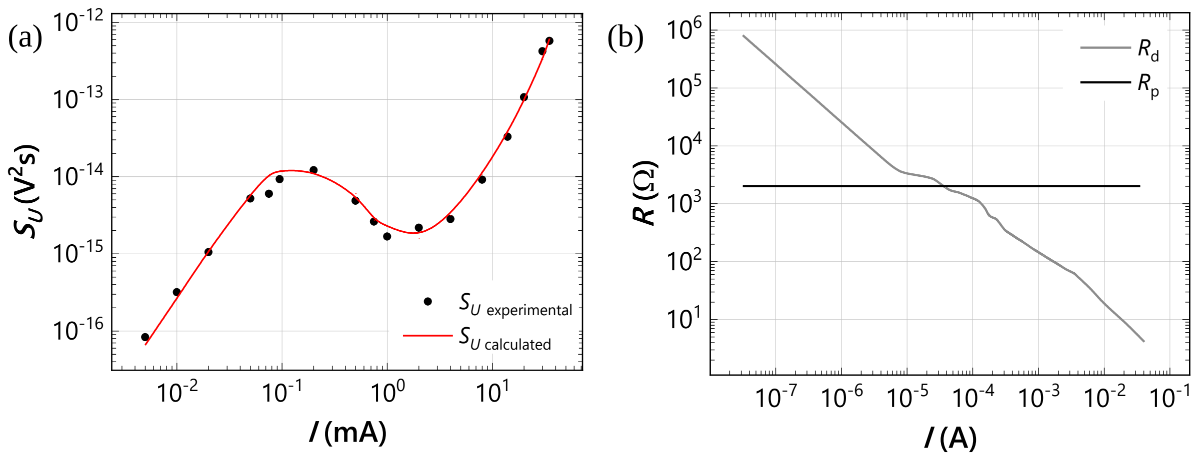


**Fig. 20.** Experimental (black dots) and calculated (red curve) voltage fluctuation spectral density (a) and calculated $R_d$ and $R_p$ resistances (b) dependences on forward current at 1 kHz frequency for investigated group 1 hydrogenated graphene/Si junction.

Based on the proposed equivalent circuit, the total output electrical noise spectral density $S_{U\ \mathrm{out}}$ was expressed as the sum of contributions from two independent noise sources $u_{R_{\mathrm{S}\ 1/f}}$ and $u_{R_{\mathrm{p}\ 1/f}}$:

$$S_{U\ \mathrm{out}} = S_{U\ R\mathrm{p}\ 1/f} + S_{U\ R\mathrm{s}\ 1/f}, \tag{15}$$

1/*f* noise intensity due to fluctuations arising from the noise sources located in parallel ohmic resistance can be calculated as: The 1/*f* noise contribution associated with the parallel resistance was expressed as:

$$S_{U\ R\mathrm{p}\ 1/f} = \frac{AU^2}{f}\left(\frac{R_\mathrm{d}}{\mathrm{R_p} + R_\mathrm{d}}\right)^2, \tag{16}$$

and with the series resistance as:

$$S_{U\ R\mathrm{s}\ 1/f} = \frac{B}{f} \cdot I^{\gamma}, \tag{17}$$

where $\gamma \approx 2.5$, $A$, $B$ – coefficients, $f$ – frequency. As can be seen in Fig. 20 (a), the noise source $u_{R_{\mathrm{S}\ 1/f}}$ dominates only above 3 mA. The index $\gamma$ in Eq. (17) exceeds 2, however, for purely contact-related noise, quadratic current dependence $S_U \sim I^2$ is expected. [55]. This suggest that the noise contribution at high current cannot be solely attributed to contact noise. However, at high bias, the current crowding effect also takes place and influences this dependence and the index $\gamma$, similarly as for samples with h-BN interlayers.

The experimentally measured and calculated $S_U$ dependences on current at 1 kHz are compared in Fig. 20 (a). The characteristic "bump"-like behaviour is explained by the interplay between the differential resistance $R_\mathrm{d}$ and the parallel resistance $R_\mathrm{p}$ (Fig. 20 (b)). In the low current interval, where

I-V characteristic remains linear (up to ~0.05 mA), $R_d$ is sufficiently large and the noise spectral density increases with current as $I^2$. With increasing current $R_d$ decreases and eventually shunts the parallel resistance $R_p$, reducing the contribution of its corresponding noise source $u_{R_{p\,1/f}}$. Thus, noise intensity decreases in the current interval up to 3 mA, beyond which noise contribution associated with the series resistance becomes dominant.

The model reproduces the observed behaviour, including the pronounced “bump”, with a close agreement between calculated and experimental dependences. This demonstrates that the two noise sources are sufficient to explain the observed noise behaviour in the investigated junction ($H_2/CH_4$ = 80/70). It also shows that within the investigated current range the noise contribution from pure thermionic emission is significantly lower than the noise associated with $u_{R_{p\,1/f}}$ noise source [8].

## 3.2. Investigation of graphene field-effect transistors

### 3.2.1. Typical output characteristics at zero gate voltage

Firstly, measurements of transistor output characteristics, i.e. drain current ($I_{ds}$) dependence on drain-source voltage ($U_{ds}$) have been performed when gate voltage is zero ($U_g = 0$), for all investigated samples. An example is represented in Fig. 21. For all investigated gFETs, this characteristic is nearly linear and does not depend on $U_{ds}$ polarity. Electrical noise exhibits 1/*f* behaviour for all $U_{ds}$ values in the investigated voltage and frequency ranges (Fig. 22 (a)). To determine whether 1/*f* noise originates from resistance fluctuations, the noise spectral density was plotted as a function of $U_{ds}$ (Fig. 22 (b)). The observed quadratic dependence on applied voltage confirms this assumption. This linear output characteristic differs from that of a regular FET, in which saturation mode is reached when the drain current becomes independent of the drain-source voltage. In [56], it is presented that linear gFET behaviour is usually due to a highly doped graphene, while the nonlinear behaviour is strongly related to the graphene localized carrier densities and their non-uniformity.

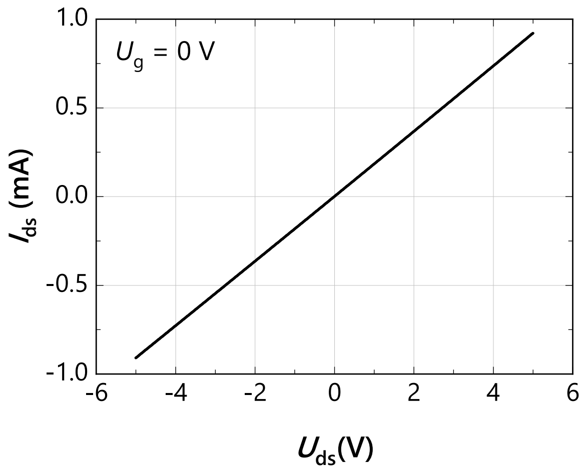


**Fig. 21.** An example of drain current dependence on drain-source voltage, when $U_g$ = 0 V (762 sample).

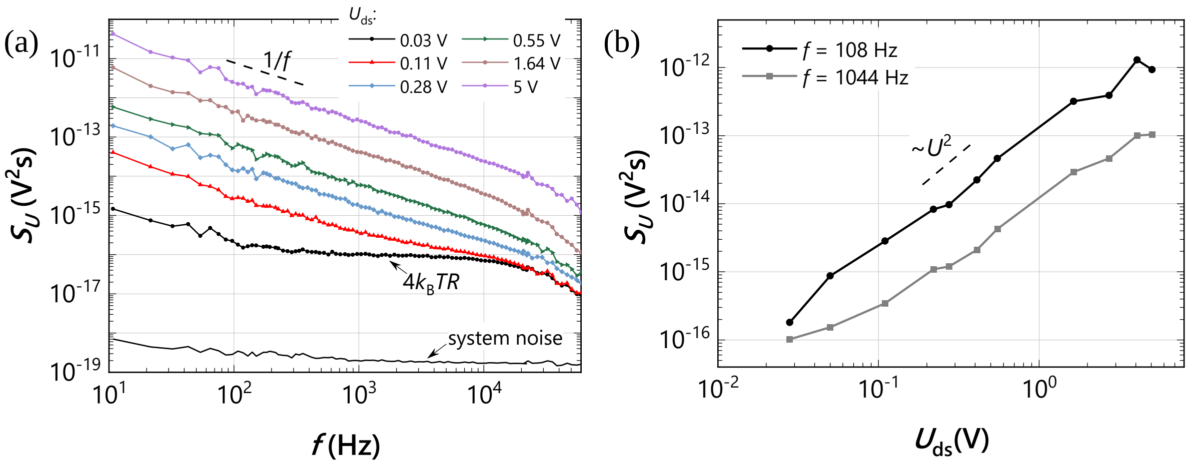


**Fig. 22.** Electrical noise spectra at different drain-source voltage values, when $U_g$ = 0 V (762 sample); $4k_BTR$ denotes the thermal noise level, where $R$ is gFET channel resistance (a); an example of voltage noise spectral density dependence on drain-source voltage (b).

### 3.2.2. Typical transfer characteristic of graphene FET

The typical transfer characteristic of the investigated gFET is represented in Fig. 23. In ideal graphene, the Dirac point lies exactly at the Fermi level and corresponds to zero carrier density, meaning that the number of electrons equals the number of holes. This point represents the charge neutrality point (CNP) where conductivity is minimal [11]. Thus, the Dirac voltage (or $U_{CNP}$) can be determined from the transfer characteristic as the voltage at which $I_{ds}$ reaches minimum (resistance reaches maximum), with the curve typically exhibiting a “V” shape. However, in the examined samples, the Dirac point is strongly shifted from zero gate bias, indicating intrinsic graphene doping. This shift is usually due to the adsorption of atmospheric species such as $H_2O$ and $O_2$, which act as hole dopants [11], or due to substrate-induced doping and defects or charged impurities at the graphene/$SiO_2$ interface, which can lead to n-type doping [4]. The exact causes of the Dirac point shift will be discussed in Section 3.2.5. In [36] it was demonstrated that h-BN flakes transferred on $SiO_2$ substrate result in the shift of the Dirac voltage of the graphene subsequently transferred on top. As a result, gFETs with the h-BN substrate would have a lower Dirac voltage compared to that fabricated directly on the $SiO_2$ substrate.

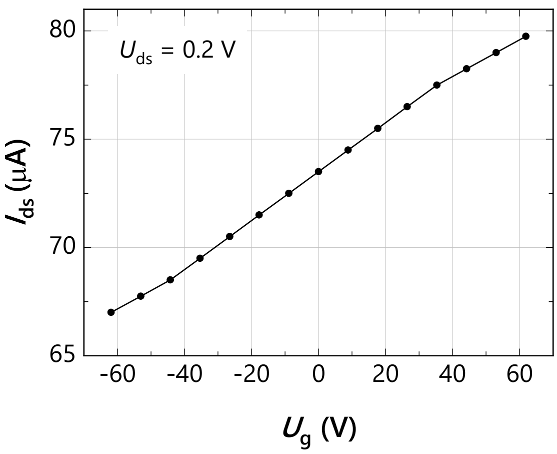


**Fig. 23.** An example of drain current ($I_{ds}$) dependence on gate voltage ($U_g$) at $U_{ds}$ = 0.2 V (771 sample).

### 3.2.3. Electrical noise characteristics of gFETs

Electrical noise spectra of the investigated gFETs are 1/*f*-type at different positive and negative gate voltage values (Fig. 24). Compared to the electrical fluctuations of graphene/Si junctions (especially samples with hydrogenated graphene), no clear Lorentzian noise components were observed in the investigated gFETs. However, the noise of some of the gFET samples at certain gate voltages is characterized by a random telegraph signal (RTS) with different characteristic time constants, which is observed in the noise signal time domain (Fig. 25). As these time constants are different and widely separated in time, and the intensity of RTS is relatively low, the electrical noise spectrum of such signal remains 1/*f*-type with only small bulges. Otherwise, clear Lorentzian-type components of high intensity would be observed.

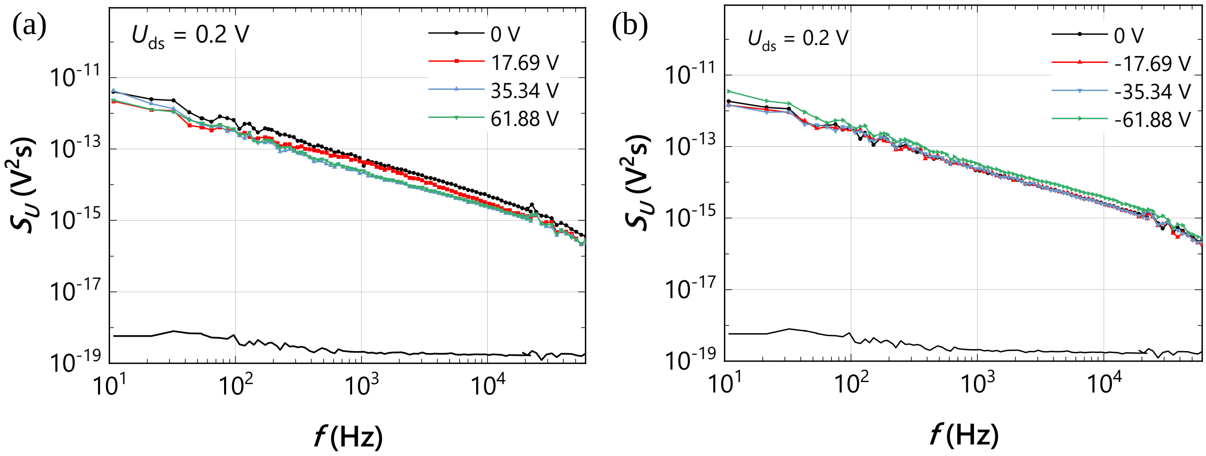


**Fig. 24.** Electrical noise spectra at different positive (a) and negative (b) gate voltages at $U_{ds}$ = 0.2 V (771 sample).

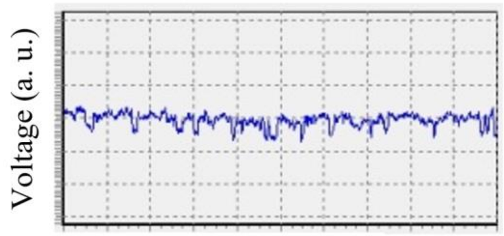


**Fig. 25.** Electrical noise signal in the time domain in the noise measurement program window (here the bandwidth is set from 10 Hz to 20 kHz, $U_g$ = 63 V, $U_{ds}$ = 0.2 V) (769 sample).

Voltage noise spectral densities were recalculated to current noise spectral densities in order to compare the obtained gate voltage dependencies with the literature. The normalized current noise spectral density ($S_I/I_{ds}^2$, $I_{ds}$ is drain current) dependence on gate voltage is very weak (Fig. 26). In conventional transistors, the lack of gate-bias dependence or the increase of $S_I/I_{ds}^2$ with rising $U_g$ would indicate that the noise is primarily governed by contributions from the ungated regions of the device or from the contacts or it is due to non-homogeneous trap distribution in energy or space [57]. If, instead, the noise originates from the gated channel, the normalized spectral density would be expected to decrease with increasing gate bias because the McWhorter model (which is usually used for MOSFET noise analysis) predicts that the $S_I/I_{ds}^2$ decreases in the strong inversion regime as ~ $1/n^2$ (where $n$ is the channel carrier's concentration) [57]. However, for gFETs, different scenarios can be expected. Usually, if the Dirac voltage is observed in the measurement voltage range, normalized noise is expected to exhibit a "V" or "M" shape dependence on the gate voltage. On the other hand, there is a scientific report where no or weak noise dependence on the gate voltage has also been observed [58]. Thus, it is important to determine the underlying reasons.

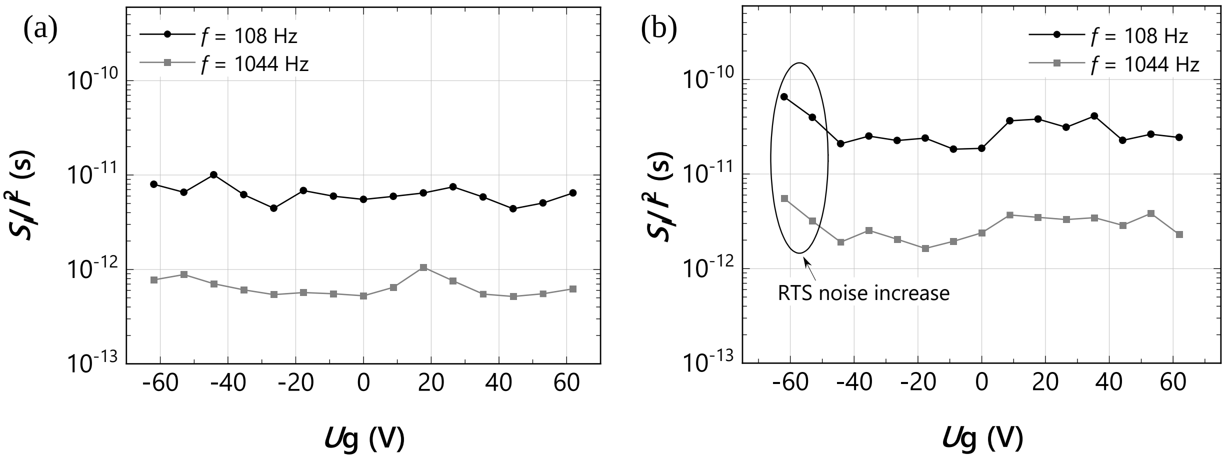


**Fig. 26.** Examples of normalized current noise spectral density dependences on negative and positive gate voltage at $U_{\mathrm{ds}}$ = 0.2 for 771 sample (a) and 769 sample (b) at different frequencies.

In the investigated gFETs, the change in channel carrier concentration (and, consequently, drain current) induced by applied the gate voltage is sufficiently abrupt for the noise level to change drastically only solely due to channel resistance variance. No apparent dependence of the appearance of RTS noise on gate voltage has been observed. However, these RTS fluctuations lead to a noticeable increase in noise intensity (Fig. 26 (b)). This suggests that low-frequency fluctuations cannot be considered to originate only from contacts because, since in that case the RTS noise behaviour would be expected to be the same or very similar among different samples within the same group. Defects, various imperfections or impurities can be located inside the graphene layer, at the graphene/$SiO_2$ interface, or inside the gate oxide. This implies that at a particular gate voltage, the contributions from the graphene irregularities, such as flakes or wrinkles, and from the bulk of the gate oxide are significant. This means that improving oxide quality, surface cleaning, and passivation are also important factors in reducing the electrical noise level in graphene FETs. This is also confirmed by the dependence of the normalized voltage noise spectral density on the resistance $R$ (drain to source resistance – the sum of channel and contact resistances at zero gate voltage), which is presented in Fig. 27 for all investigated transistors. It is expected that $S_U/U^2$ (or $S_R/R^2$) scales as $R^3$ for $1/f$ fluctuations originating from the bulk in conventional metals and semiconductors, and for interface-dominated contact noise $S_U/U^2 \sim R$. What is more, for multi-spot contact noise the proportionality is also $S_U/U^2 \sim R^3$ [6]. However, for the investigated graphene FETs, only for the 771 and 772 group samples, dependencies can be observed close to $S_U/U^2 \sim R^3$ (Fig. 27). Trapped charge at the $SiO_2$ surface can cause contact noise, and defect formation can strongly influence the band structure of graphene underneath the metal, as shown in [44]. Thus, these individual fluctuators can affect the conductance locally over a small area with the RTS noise appearance and distort the dependences in

Fig. 27. Also, large channels of the investigated gFETs are more susceptible to extrinsic scattering from charged impurities and surface inhomogeneities [4].

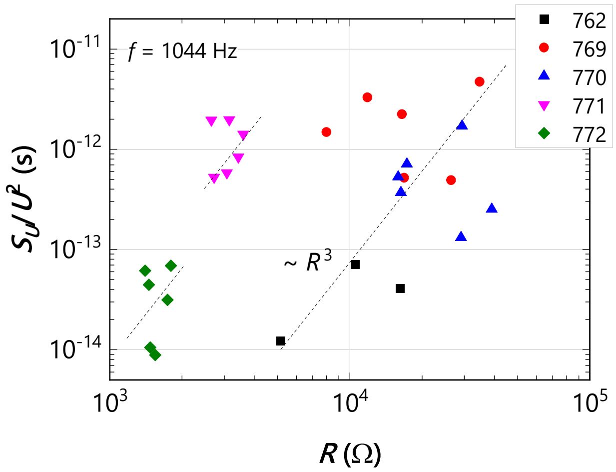


**Fig. 27.** Dependence of the normalized voltage noise spectral density on drain to source resistance for all investigated samples at zero gate voltage at 1044 Hz frequency.

The reasons for the differences in noise intensity between gFET samples with different graphene synthesis conditions will be discussed in Section 3.2.5, where a statistical investigation of multiple samples has been performed.

### 3.2.4. Statistical investigation of graphene/Si junctions

To compare the noise intensity between different junctions, voltage noise spectral density values at 1044 Hz have been extracted for multiple investigated samples within each investigated junction category (6 samples of each graphene/h-BN/Si h-BN thickness group and 5 samples of each hydrogenated graphene/Si group). Here, 0.02 mA current is chosen as it corresponds to the linear regions of the I-V characteristics.

It is important to evaluate the impact of h-BN interlayer thickness on the graphene/h-BN/Si junctions through the low-frequency noise characterization. As a general trend, junctions with a 5 nm-thick h-BN interlayer demonstrated the highest noise intensity, and the average noise level is not directly proportional to the h-BN thickness (Fig. 28 (a)). Non-monotonic noise increase with the defect density in graphene is also observed (inset in Fig. 28 (a)). Initially, the noise clearly increases with the *I*(D)/*I*(G) ratio. However, for samples featuring an inserted 1 nm-thick h-BN interlayer, a significant reduction in the noise level is observed. To identify possible reasons for this inconsistency, the effects of different graphene defect types were investigated. In the case of the graphene/h-BN/Si junctions containing 3 nm, 5 nm, and 15 nm thickness boron nitride interlayers, the *I*(D)/*I*(D’) value was about 2.5 (Fig. 28 (b)). That is between the value typical for grain boundary defects (3.5) and the value typical for on-site defects (1.3), which are commonly linked to hydrogen species bonded to the graphene [49]. In the case of the reference graphene sample, grain boundary defects also prevail. However, considering these $I(D)/I(D')$ values, the presence of some on-site defects is observed. For samples with an inserted 1 nm thickness h-BN interlayer, the $I(D)/I(D')$ value appears to nearly match the typical value for grain boundaries (~3.6). The presence of some hydrogen bonds was revealed in HIPIMS-deposited h-BN films grown using Raman spectroscopy [59]. In HIPIMS, hydrogen can originate from residual water vapor or hydrocarbons in the chamber; these species are dissociated in plasma and become bonded to boron or nitrogen at the growing film's surface [59]. Such hydrogen incorporated in the h-BN layer could subsequently be released during the graphene's direct synthesis step and become incorporated into the growing graphene. For the 1 nm h-BN film, the absence of detectable hydrogen-related features in the graphene suggests that either hydrogen was initially negligible, or it was fully desorbed during synthesis. For thicker h-BN interlayers, hydrogen atoms could diffuse from the boron nitride into the graphene layer during growth, becoming incorporated into its structure.

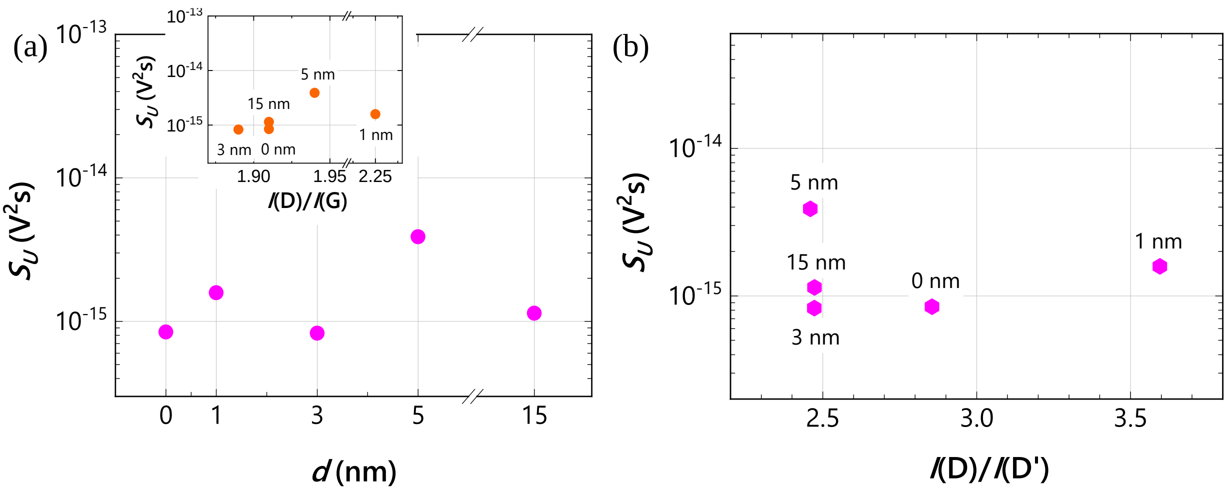


**Fig. 28.** Dependences of average voltage noise spectral density at forward currents of 0.02 mA at 1044 Hz frequency on h-BN layer thickness *d* (a) and $I(D)/I(D')$ ratio. Inset in (a) shows average voltage noise spectral density dependence on $I(D)/I(G)$ ratio.

A statistical analysis has been also performed on multiple junctions from each of the hydrogenated graphene/Si junction group to assess whether a relationship exists between the averaged electrical noise level and the $H_2/CH_4$ flow ratio (Fig. 29). The results show that electrical noise level increases with $H_2/CH_4$ flow ratio and is consistent with a higher defect density in graphene and its interfaces within the investigated junctions. As Raman spectra measurements reveal, the dominant defects are on-site defects ($I(D)/I(D') \approx 1.15$), which are hydrogen-related. Only the group 3 junctions exhibit a higher density of grain boundaries ($I(D)/I(D') \approx 1.76$) [8].

Statistical analysis of all investigated graphene-based junctions represents the importance of H-related defects in graphene/Si samples synthesized using PECVD.

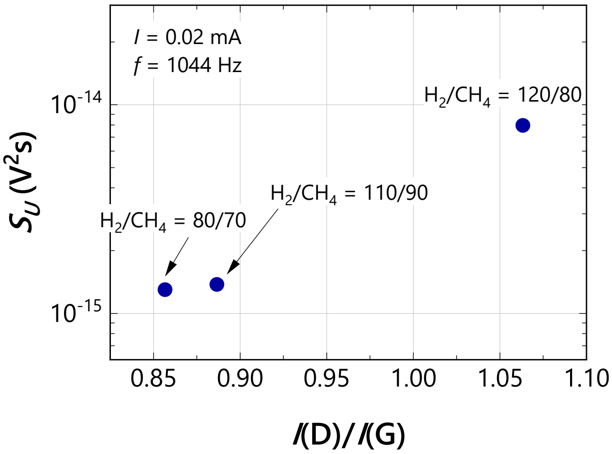


**Fig. 29.** Average voltage noise spectral density vs. *I*(D)/*I*(G) ratios. The $S_U$ was measured at a forward current of 0.02 mA and at a frequency of 1044 Hz.

### 3.2.5. Statistical investigation of gFETs

A statistical analysis has been performed on six different gFETs from each of the sample groups (for the 762 sample group, three gFETs were analyzed) in order to find the relationship between noise intensity and graphene properties. An interesting tendency was observed – average electrical noise level decreases while defect density (represented by *I*(D)/*I*(G) ratio) increases in graphene (Fig. 30 (a)). This is the opposite of the observed dependence in the hydrogenated graphene/Si junctions as discussed earlier (Fig. 29). Furthermore, the average drain to source resistance of gFETs also decreases with the *I*(D)/*I*(G) ratio increasing. A similar phenomenon has been observed in [60], where the low-frequency noise level decreases in gFETs after the low-energy electron-beam irradiation. However, after the irradiation, the defect density and the total number of the carrier mobility scattering centers increases. As shown in Fig. 30 (b) and Fig. 27, the density of free charge carriers in the channel increases (the resistance decreases) with increasing defect density in graphene. This can only be the case if these defects have very low excitation energy and act as dopants in graphene. As a result, the 1/*f* noise intensity is inversely proportional to the number of charge carriers in the device, and therefore, the observed noise dependence can be explained. In the investigated samples, the ratio *I*(D)/*I*(D’) is between 3.2 and 4.3, which shows that the dominant defects are grain boundaries. An increased charge density can be found at grain boundaries [61], which is an additional explanation for why the noise intensity dependence on the *I*(D)/*I*(G) ratio differs in hydrogenated graphene junctions, where on-site defects are dominant. From graphene Raman spectral analysis, it is well known that the combination of a downshift in Pos(2D) and an upshift in Pos(G) (Fig. A5 (a)) is characteristic of n-type doping in graphene [4]. The n-type doping is due to unintentional self-doping arising from interactions with the substrate when charged impurities at the interface transfer electrons to the graphene, shifting its Fermi level [3, 4, 21]. This also explains the Dirac shift observed in the transfer characteristic.

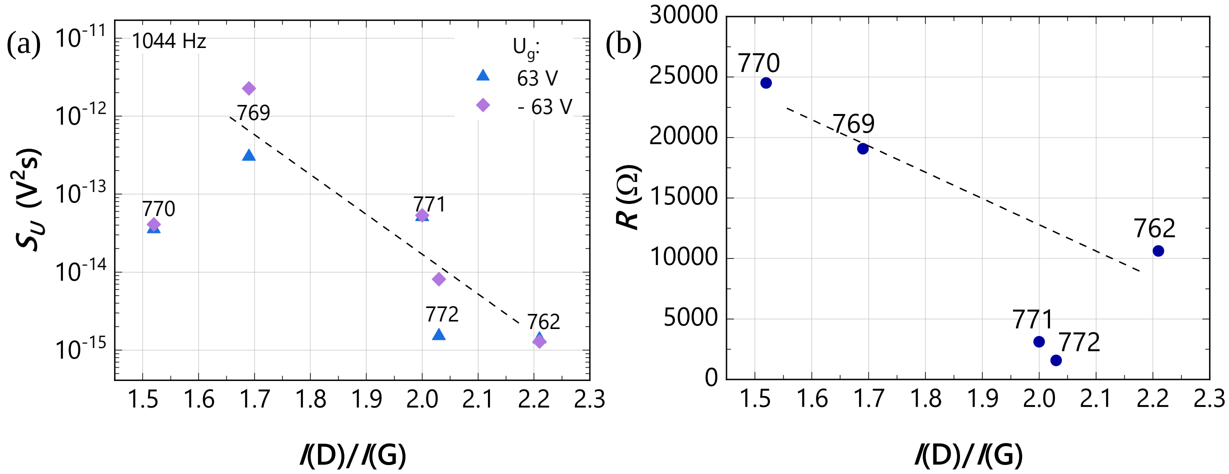


**Fig. 30.** Average voltage noise spectral density vs. $I$(D)/$I$(G) ratio (a) and average drain to source resistance vs. $I$(D)/$I$(G) ratio (b) of different sample groups. Averaged $S_U$ values are at positive and negative gate voltages of 63 V at 1044 Hz frequency. Dashed lines are eye-guides to demonstrate the observed tendencies.

As Fig. 31 shows, the electrical noise level decreases with the increase in the number of graphene layers ($I$(2D)/$I$(G) ratio decreases with the increase in the number of graphene layers). Graphene's n-type self-doping rises with increasing thickness because in thicker graphene stacks, the injected charge is distributed among more layers, which allows the increase of the total doping level [4]. Thus, the observed noise dependence on $I$(2D)/$I$(G) can be explained similarly as Fig. 30 (a).

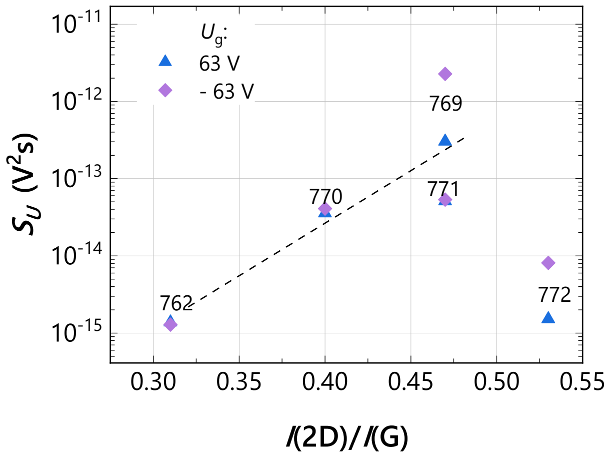


**Fig. 31.** Average voltage noise spectral density vs. $I$(2D)/$I$(G) ratio of different sample groups. Averaged $S_U$ values are at positive and negative gate voltages of 63 V at 1044 Hz frequency. Dashed line is an eye-guide to demonstrate the observed tendency.

As Fig. 31 represents, the 771 and especially the 772 group, where graphene was synthesized at higher temperatures, deviates from the observed trend and exhibits a lower noise level. This can be due to the onset of vertical graphene growth at elevated temperature [4], which leads to multi-spot graphene contact formation as proportionality $S_U/U^2 \sim R^3$ in Fig. 27 shows. This results in significantly lower resistance (Fig. 30 (b)) and, as a consequence, lower noise intensity.

# Conclusions

1. All investigated graphene/h-BN/Si and the reference sample junctions distinguished by $1/f$ or $1/f^{\alpha}$-type voltage noise spectra. Hydrogenated graphene/Si junctions exhibited $1/f$, Lorentzian, or both types of voltage noise spectra, depending on the $H_2/CH_4$ flow ratio used during low-temperature PECVD growth of graphene.

2. Graphene FETs are characterized by $1/f$ fluctuations with the appearance of RTS noise at a particular gate voltage.

3. Hydrogenated/Si junctions exhibit an unusual bump-like noise dependence on current, while all investigated graphene junctions exhibit a rapid noise growth ($\sim I^{\gamma}$, where $\gamma > 2$) at high forward bias due to grain boundaries as noise sources and current crowding effect.

4. The statistical analysis of multiple samples across each h-BN layer thickness category, combined with analysis of graphene Raman spectra, revealed the highest noise level in samples with a 5 nm layer thickness due to hydrogen-related defects. The trap level responsible for the observed Lorentzian-type fluctuations with an activation energy of 0.4 eV in hydrogenated graphene samples is consistent with hydrogen or hydroxyl related defects.

5. Unintentional graphene substrate-induced n-type self-doping has a huge influence on the investigated graphene FETs' noise intensity.

## References


[1] B. Vamsi Krsihnaa, S. Ravib, M. Durga Prakash, „Recent developments in graphene based field effect transistors“, *Materials Today: Proceedings*, vol. 45, pp. 1524–1528, 2021.

[2] X. Kong, L. Zhang, B. Liu, H. Gao, Y. Zhang, H. Yan, X. Song, "Graphene/Si Schottky solar cells: a review of recent advances and prospects", *RSC Advances*, vol. 9, no. 2, pp. 863–877, 2019.

[3] R. Gudaitis, A. Lazauskas, Š. Jankauskas, Š. Meškinis, "Catalyst-less and transfer-less synthesis of graphene on Si(100) using direct microwave plasma-enhanced chemical vapor deposition and protective enclosures", *Materials*, vol. 13, no. 24, 2020.

[4] Š. Meškinis, Š. Jankauskas, L. Kamarauskas, A. Vasiliauskas , A. Guobiene, A. Lazauskas, R. Gudaitis, "Effect of Synthesis Conditions on Graphene Directly Grown on $SiO_2$: Structural Features and Charge Carrier Mobility", *Nanomaterials*, vol. 15, 1315, 2025.

[5] M. A. Rehman, I. Akhtar, W. Choi, K. Akbar, A. Farooq, S. Hussain, M. A. Shehzad, S.-H. Chun, J. Jung, Y. Seo, „Influence of an $Al_2O_3$ interlayer in a directly grown graphene silicon Schottky junction solar cell“, *Carbon*, vol. 132, pp. 157–164, 2018.

[6] L. K. J. Vandamme, „Noise as a diagnostic tool for quality and reliability of electronic devices“, *IEEE Transactions on Electron Devices*, vol. 41, no. 11, pp. 2176–2187, 1994.

[7] I. Pliaterytė "Low-frequency noise characteristics of graphene/h-BN/Si junctions", Master's scientific research work, Vilnius, Lithuania, 2025, 29 p.

[8] I. Pliaterytė „Low-frequency noise characteristics of hydrogenated graphene/Si junctions“, Master‘s scientific research work, Vilnius, Lithuania, 2026, 35 p.

[9] G. Dash, S. R. Pattanaik, S. Behera, "Graphene for Electron Devices: The Panorama of Decade", *IEEE Journal of the Electron Devices Society*, vol. 2, pp. 77–104, 2014.

[10] Z. Ma, Z. Geng, Z. Fan, J. Liu, H. Chen, "Modulators for Terahertz Communication: The Current State of the Art", *Research*, vol. 2019, pp. 1–22, 2019.

[11] J. P. Nayak, S. Sahoo, S. Barman, G. N. Daptary, „Low-Frequency Noise as a Probe of Microscopic Disorder in Chemical Vapor Deposition-Grown Graphene“, *Physica status solidi (a)*, vol. 223, e70330, 2026.

[12] S. Ahmed, F. Altaf, R. K. Manavalan, R. K. Dharman, K. Naseem, J. Khan, B. Miao, S. Y. Kim, H. Zhang, J. S. Ponraj, „Functionalization, properties and applications of hydrogenated two-dimensional materials“, *Transactions of Tianjin University*, vol. 31, pp. 205–269, 2025.

[13] A. Savchenko, „Transforming graphene“, *Science*, vol. 323, pp. 589–590, 2009.

[14] J. S. Burgess, B. R. Matis, J. T. Robinson, F. A. Bulat, F. Keith Perkins, B. H. Houston, J. W. Baldwin, „Mechanical properties and nanostructure of carbon materials“, *Carbon*, vol. 49, pp. 4420–4428, 2011.

[15] X. Wang, G. Shi, „An introduction to the chemistry of graphene“, *Physical Chemistry Chemical Physics*, vol. 17, pp. 28484–28504, 2015.

[16] J. Cong, A. Khan, P. Hang, L. Cheng, D. Yang, X. Yu, „High detectivity graphene/Si heterostructure photodetector with a single hydrogenated graphene atomic interlayer for passivation and carrier tunneling“, *Nanotechnology*, vol. 33, 505201, 2022.

[17] V. Jain, B. Kandasubramanian, "Functionalized graphene materials for hydrogen storage", *Journal of Material Science*, vol. 55, pp. 1865–1903, 2020.

[18] J. Zhou, Q. Wang, Q. Sun, X. S. Chen, Y. Kawazoe, P. Jena, "Electronic and structural properties of graphene-based low-dimensional systems", *Nano Letters*, vol. 9, pp. 3867–3870, 2009.

[19] S. Deng, V. Berry, “Wrinkled, rippled and crumpled graphene: an overview of formation mechanism, electronic properties, and applications”, *Materials Today*, vol. 19, pp. 197–212, 2016.

[20] M. Li, D. Liu, D. Wei, X. Song, D. Wei, A. Thye, S. Wee, „Controllable synthesis of graphene by plasma-enhanced chemical vapor deposition and its related applications“, *Advanced Science*, vol. 3, 1600003, 2016.

[21] Š. Meškinis, A. Lazauskas, Š. Jankauskas, A. Guobienė, R. Gudaitis, „Advancing graphene synthesis: low-temperature growth and hydrogenation mechanisms using plasma-enhanced chemical vapor deposition“, *Molecules*, vol. 30, 33, 2025.

[22] A. K. Jehad, M. Yurddaskal, F. Gunes, C. Zafer, K. Kocabas, “Investigation of graphene-based Schottky junction solar cell with heavy-doped silicon”, *Journal of Materials Science: Materials in Electronics*, vol. 32, no. 24, pp. 28856–28869, 2021.

[23] J. Fu, C. Nie, F. Sun, G. Li, X. Wei, “Photodetectors based on graphene–semiconductor hybrid structures: recent progress and future outlook”, *Advanced Devices & Instrumentation*, vol. 4, 0031, 2023.

[24] H. Yang, J. Heo, S. Park, H. J. Song, D. H. Seo, K.-E. Byun, P. Kim, I. K. Yoo, H.-J. Chung, K. Kim, “Graphene barristor, a triode device with a gate controlled Schottky barrier”, *Science*, vol. 336, no. 6085, pp. 1140–1143, 2012.

[25] Y. An, A. Behnam, E. Pop, G. Bosman, A. Ural, “Forward bias diode parameters, electronic noise, and photoresponse of graphene/silicon Schottky junctions with an interfacial native oxide layer”, *Journal of Applied Physics*, vol. 118, no. 11, 114307, 2015.

[26] G. Kalita, M. Kobayashi, M. D. Shaarin, R. D. Mahyavanshi, M. Tanemura, “Schottky Barrier Diode Characteristics of Graphene-GaN Heterojunction with Hexagonal Boron Nitride Interfacial Layer”, *Physica Status Solidi A*, vol. 215, 1800089, 2018.

[27] J.-H. Meng, X. Liu, X.-W. Zhang, Y. Zhang, H.-L. Wang, Z.-G. Yin, Y.-Z. Zhang, H. Liu, J.-B. You, H. Yan, “Interface engineering for highly efficient graphene-on-silicon Schottky junction solar cells by introducing a hexagonal boron nitride interlayer”, *Nano Energy*, vol. 28, pp. 44–50, 2016.

[28] S. M. Sze, Physics of Semiconductor Devices, 2nd ed., New York, NY, USA: John Wiley & Sons, Inc., 1981.

[29] S. M. Sze, M. K. Lee, *Semiconductor Devices*, 3rd ed., Hoboken, NJ, USA: John Wiley & Sons, Inc., 2012.

[30] C. P. Kwan, M. Street, A. Mahmood, et al., „Space-charge limited conduction in epitaxial chromia films grown on elemental and oxide-based metallic substrates“, *AIP Advances*, vol. 9, 055018, 2019.

[31] Z. Çaldıran, M. Şinoforoğlu, Ö. Metin, et al., „Space charge limited current mechanism in graphene oxide–$Fe_3O_4$ nanocomposites/n-Si heterojunctions“, *Journal of Alloys and Compounds*, vol. 631, pp. 261–265, 2015.

[32] A. P. Singh, P. N. Shankar, RK. Baghel, S. Tirkey, „A Review on Graphene Transistors“, *IEEE* International Students' Conference on Electrical, Electronics and Computer Science (SCEECS), Bhopal, India, 2023.

[33] F. Xia, D. B. Farmer, Y. Lin, P. Avouris, „Graphene Field-Effect Transistors with High On/Off Current Ratio and Large Transport Band Gap at Room Temperature“, *Nano Letter*, vol. 10, pp. 715-718, 2010.

[34] A. K. Geim, K. S. Novoselov, „The rise of graphene“, *Nature materials*, vol. 6, pp. 183-191, 2007.

[35] F. Pasadas, A. Medina-Rull, F. G. Ruiz, J. N. Ramos-Silva, A. Pacheco-Sanchez, M. C. Pardo, A. Toral-Lopez, A. Godoy, E. Ramírez-García, D. Jiménez, E. G. Marin, „Exploiting Ambipolarity in Graphene Field-Effect Transistors for Novel Designs on High-Frequency Analog Electronics“, *Small*, vol. 19, 2303595, 2023.

[36] O. Sul, K. Kim, Y. Jung, E. Choi, S.-B. Lee, „Selective Dirac voltage engineering of individual graphene field-effect transistors for digital inverter and frequency multiplier integrations“, *Nanotechnology*, vol. 28, 37LT01, 2017.

[37] F. N. Hooge, T. G. M. Kleinpenning, L. K. J. Vandamme, “Experimental studies on 1/*f* noise”, *Reports on Progress in Physics*, vol. 44, no. 5, pp. 479–532, 1981.

[38] M. J. Kirton, M. J. Uren, “Noise in solid-state microstructures: A new perspective on individual defects, interface states and low-frequency (1/*f*) noise”, *Advances in Physics*, vol. 38, no. 4, pp. 367–468, 1989.

[39] F. Banhart, J. Kotakoski, A. V. Krasheninnikov, “Structural defects in graphene,” *ACS Nano*, vol. 5, no. 1, pp. 26–41, 2011.

[40] M. D. Bhatt, H. Kim, G. Kim, “Various defects in graphene: a review”, *RSC Advances*, vol. 12, no. 33, pp. 21520–21547, 2022.

[41] Kochat, C. S. Tiwary, T. Biswas, G. Ramalingam, K. Hsieh, K. Chattopadhyay, S. Raghavan, M. Jain, A. Ghosh, “Magnitude and Origin of Electrical Noise at Individual Grain Boundaries in Graphene”, *Nano Letters*, vol. 16, no. 1, pp. 562–567, 2016.

[42] A. A. Balandin, “Low-frequency 1/*f* noise in graphene devices”, *Nature Nanotechnology*, vol. 8, no. 8, pp. 549–555, 2013.

[43] Y. M. Lin, P. Avouris, “Strong suppression of electrical noise in bilayer graphene nanodevices”, *Nano Letters*, vol. 8, pp. 2119–2125, 2008.

[44] P. Karnatak, T. P. Sai, S. Goswami, S. Ghatak, S. Kaushal, A. Ghosh, “Current crowding mediated large contact noise in graphene field-effect transistors”, *Nature Communications*, vol. 7, 13703, 2016.

[45] J. Shen, X. Liu, X. Song, X. Li, J. Wang, Q. Zhou, S. Luo, W. Feng, X. Wei, S. Lu, S. Feng, C. Du, Y. Wang, H. Shi, D. Wei, “High-performance schottky heterojunction photodetector with directly grown graphene nanowalls as electrodes”, *Nanoscale*, vol. 9, pp. 6020-6025, 2017.

[46] X. Li, M. Zhu, M. Du, Z. Lv, L. Zhang, Y. Li, Y. Yang, T. Yang, X. Li, K. Wang, H. Zhu, Y. Fang “High detectivity graphene-silicon heterojunction photodetector”, *Small*, vol. 12, pp. 595-601, 2016.

[47] M. Zhu, X. Li, X. Li, X. Zang, Z. Zhen, D. Xie, Y. Fang, H. Zhu, “Schottky diode characteristics and 1/*f* noise of high-sensitivity reduced graphene oxide/Si heterojunction photodetector”, *Journal of Applied Physics*, vol. 119**,** 124303, 2016.

[48] Childres, L. A. Jauregui, J. Tian, Y. P. Chen, “Effect of oxygen plasma etching on graphene studied using Raman spectroscopy and electronic transport measurements”, *New Journal of Physics*, vol. 13, 025008, 2011.

[49] A. Eckmann, A. Felten, A. Mishchenko, L. Britnell, R. Krupke, K. S. Novoselov, C. Casiraghi, “Probing the nature of defects in graphene by Raman spectroscopy”, *Nano Letters*, vol. 12, pp. 3925–3930, 2012.

[50] Hwang, J.-S.; Lin, Y.-H.; Hwang, J.-Y.; Chang, R.; Chattopadhyay, S.; Chen, C.-J.; Chen, P.; Chiang, H.-P.; Tsai, T.-R.; Chen, L.-C.; et al. “Imaging Layer Number and Stacking Order through Formulating Raman Fingerprints Obtained from Hexagonal Single Crystals of Few Layer Graphene”, *Nanotechnology*, vol. 24, 015702, 2012.

[51] A. Salehi-Khojin, D. Estrada, K. Y. Lin, M.-Ho Bae, F. Xiong, E. Pop, R. I. Masel, „Polycrystalline Graphene Ribbons as Chemiresistors“, *Advanced Materials*, vol. 24, pp. 53–57, 2012.

[52] B. Kumar, K. Min, M. Bashirzadeh, A. Barati Farimani, M.-H. Bae, D. Estrada, Y. D. Kim, P. Yasaei, Y. D. Park, E. Pop, N. R. Aluru, A. Salehi-Khojin, „The Role of External Defects in Chemical Sensing of Graphene Field-Effect Transistors“, *Nano Letters*, vol. 13, pp. 1962−1968, 2013.

[53] P. Wang, C. Perini, A. O'Hara, B. R. Tuttle, E. X. Zhang, H. Gong, L. Dong, C. Liang, R. Jiang, W. Liao, D. M. Fleetwood, R. D. Schrimpf, E. M. Vogel, S. T. Pantelides, "Radiation-induced charge trapping and low-frequency noise of graphene transistors**",** *IEEE Transactions on Nuclear Science*, vol. 65, pp. 156–163, 2018.

[54] R. H. Koch, J. R. Lloyd, J. Cronin, "1/*f* noise and grain-boundary diffusion in aluminum and aluminum alloys", *Physical Review Letters,* vol. 55, no. 22, pp. 2487–2490, 1985.

[55] C. H. Park, J. H. Lee, "Formulas of 1/*f* noise in Schottky barrier diodes under reverse bias", *Solid-State Electronics*, vol. 69, pp. 85–88, 2012.

[56] Rachid Fates, Jean-Pierre Raskin, "Linear and non-linear electrical behaviors in graphene ribbon based devices", *Journal of Science: Advanced Materials and Devices*, vol. 3, no. 3, pp. 366-370, 2018.

[57] Q. Shao, G. Liu, D. Teweldebrhan, A. A. Balandin, S. Roumyantesv, M. Shur, D. Yan, „Flicker Noise in Bilayer Graphene Transistors", *IEEE Electron Device Letters*, vol. 30, no. 3, pp. 288 – 290, 2009.

[58] G. Liu, W. Stillman, S. Rumyantsev, Q. Shao, M. Shur, A. A. Balandin, "Low-frequency electronic noise in the double-gate single-layer graphene transistors", *Applied Physics Letters*, vol. 95, 033103, 2009.

[59] Š. Meškinis, Š. Jankauskas, A. Vasiliauskas, V. Stankus, A. Guobienė, K. Lukoševičius, A. Jasutis, R. Gudaitis, "Graphene Direct Growth by Microwave PECVD on H-BN Films Deposited by Reactive HIPIMS", *Nano Express*, vol. 6, no. 2, 025007, 2025.

[60] S. Rumyantsev, M.S. Shur, A.A. Balandin, Md.Z. Hossain, "Reduction of the 1/*f* noise in graphene after electron-beam irradiation", *Applied Physics Letters*, vol. 102, 153512, 2013.

[61] J. Červenka, C. F. J. Flipse, "Structural and electronic properties of grain boundaries in graphite: Planes of periodically distributed point defects", *Physical Review B*, vol. 79, 195429, 2009.

# Acknowledgments

I would like to thank dr. Šarūnas Meškinis (Vacuum and Plasma Processes Research Laboratory, Institute of Materials Science, Kaunas University of Technology) for the provided samples and their documentation.

Ingrida Pliaterytė

**Grafeno sandūrinių įtaisų ir tranzistorių žemadažnio triukšmo charakteristikos**

# Santrauka

Grafenas, pasižymintis puikiomis elektrinėmis, optinėmis ir šiluminėmis savybėmis, yra patrauklus taikymams elektronikos ir optoelektronikos įtaisuose. Tiesioginis grafeno auginimas ant silicio mikrobange plazma stimuliuoto cheminio garinio nusodinimo (angl. plasma-enhanced chemical vapor deposition – PECVD) būdu leidžia išvengti sudėtingų perkėlimo procedūrų ir yra perspektyvus pramoniniam taikymui. Vis dėlto tokiu būdu augintas grafenas dažnai pasižymi struktūriniais defektais, turinčiais reikšmingą įtaką grafeno lauko tranzistorių ir sandūrinių įtaisų veikimui. Tokių struktūrų kokybei ir krūvio pernašos ypatumų analizei puikiai tinka žemadažnio triukšmo tyrimai. Iki šiol grafeno/h-BN/Si ir hidrinto grafeno sandūrų charakterizavimas naudojant žemadažnio triukšmo spektroskopiją nebuvo aprašytas mokslinėje literatūroje.

Šio darbo tikslas buvo ištirti grafeno, auginto PECVD būdu, sandūrų (grafeno/h-BN/Si ir hidrinto grafeno/Si) ir lauko tranzistorių žemadažnio triukšmo charakteristikas. Tirtos grafeno/h-BN/Si ir grafeno/Si sandūros pasižymėjo 1/*f* pobūdžio įtampos fliuktuacijų spektriniais tankiais, tuo tarpu hidrinto grafeno/Si sandūrose stebėti 1/*f*, Lorenco arba abiejų šių tipų spektriniai tankiai, priklausomai nuo grafeno sintezės metu naudoto $H_2$ ir $CH_4$ dujų srautų santykio. Visų grafeno sandūrų triukšmo spektrinių tankių priklausomybėse nuo srovės tekant didelėms srovėms stebėtas staigus triukšmo augimas ($\sim I^{\gamma}$, $\gamma > 2$), siejamas su grafeno ar h-BN sluoksniuose esančių grūdelių ribų įtaka ir srovės susitelkimo efektu. Hidrinto grafeno/Si sandūrų atveju stebėtam neįprastam tiukšmų maksimumui paaiškinti buvo pasiūlyta ekvivalentinė elektrinė grandinė su triukšmų šaltiniais. Nustatyta, kad vandenilio defektai yra reikšmingas triukšmo šaltinis tirtose sandūrose. Statistinis grafeno/h-BN/Si sandūrų su (0 – 15) nm storio h-BN tarpsluoksniais tyrimas parodė, kad intensyviausiu triukšmu pasižymėjo sandūros su 5 nm tarpsluoksniu. Siekant nustatyti hidrinto grafeno/Si sandūrose stebėtų Lorenco tipo spektrų kilmę, atlikta temperatūrinė analizė, parodžiusi, kad atsakingam krūvininkų pagavimo lygmeniui būdinga 0.4 eV aktyvacijos energija, siejama su vandenilio arba hidroksiliniais defektais. Grafeno lauko tranzistoriams buvo būdingi 1/*f* pavidalo įtampos fliuktuacijų spektriniai tankiai, o esant tam tikroms užtūros įtampoms stebėtas atsitiktinio telegrafinio signalo triukšmas. Nustatyta, kad esminę įtaką triukšmo intensyvumui daro nepageidaujamas grafeno kanalo n-tipo savaiminis legiravimasis dėl sąveikos su $SiO_2$ sluoksniu.

Ingrida Pliaterytė

**Low-frequency noise characteristics of graphene-based junctions and transistors**

## Summary

Graphene, which has excellent electrical, optical, and thermal properties, is very attractive for applications in electronic and optoelectronic devices. Direct synthesis of graphene on silicon substrate by microwave plasma-enhanced chemical vapor deposition (PECVD) benefits in avoiding complex transfer procedures and is promising for industrial applications. However, such graphene often exhibits structural defects that have a significant impact on the performance of graphene field-effect transistors and junction devices. Low-frequency noise analysis is well-suited method for the quality evaluation of such structures and the investigation of charge carrier transport. So far, no scientific reports have been found in the literature on the characterization of graphene/h-BN/Si and hydrogenated graphene junctions using low-frequency noise spectroscopy.

The aim of this work was to investigate the low-frequency noise characteristics of graphene grown by PECVD, junctions (graphene/h-BN/Si and hydrogenated graphene/Si), and field-effect transistors. The studied graphene/h-BN/Si and graphene/Si junctions were characterized by 1/*f*-type fluctuations, while in hydrogenated graphene/Si junctions, 1/*f*, Lorentzian, or both types of spectral densities were observed, depending on the ratio of $H_2$ and $CH_4$ gas flows used during the graphene synthesis. In the noise dependencies on the current for all graphene junctions, a rapid increase in noise intensity (~$I\gamma$, $\gamma > 2$) was observed at high currents, which is associated with the influence of grain boundaries in graphene or h-BN layers and the effect of current crowding. In the case of hydrogenated graphene/Si junctions, an equivalent electrical circuit with noise sources was proposed to explain the unusual noise “bump” behaviour. It was demonstrated that hydrogen-related defects are a significant noise source in the investigated junctions. Statistical analysis of graphene/h-BN/Si junctions with (0 – 15) nm thickness h-BN interlayers revealed the highest noise intensity in junctions with a 5 nm h-BN interlayer. In order to determine the origin of the Lorentzian-type spectra in hydrogenated graphene/Si junctions, a temperature-dependent noise analysis was performed, which showed that the observed trap level with the activation energy of 0.4 eV is due to hydrogen or hydroxyl-related defects. Graphene field-effect transistors were characterized by 1/*f*-type electrical fluctuations, and at certain gate voltages, a random telegraph noise signal was observed. It was found that the unintentional n-type self-doping of the graphene due to interaction with the $SiO_2$ layer has a significant impact on the investigated graphene transistors’ noise intensity.

# Appendix

### Low-frequency noise characteristics of graphene/Si junctions at reverse bias

Investigated graphene/Si junctions with or without h-BN interlayer are characterized by 1/*f*-type fluctuations over the whole investigated reverse current range (Fig. A1 (a)). Several differences are observed in hydrogenated graphene/Si sample groups spectra at reverse bias (Fig. A1 (b)). Sample groups 1 and 2 exhibit 1/*f*-type fluctuations across the entire range of investigated reverse bias. In contrast, group 3 samples show Lorentzian-type spectra at the lowest reverse currents (illustrated by 0.05 mA and 0.1 mA curves in Fig. A1 (b)). At higher bias, 1/*f*-type spectra dominate.

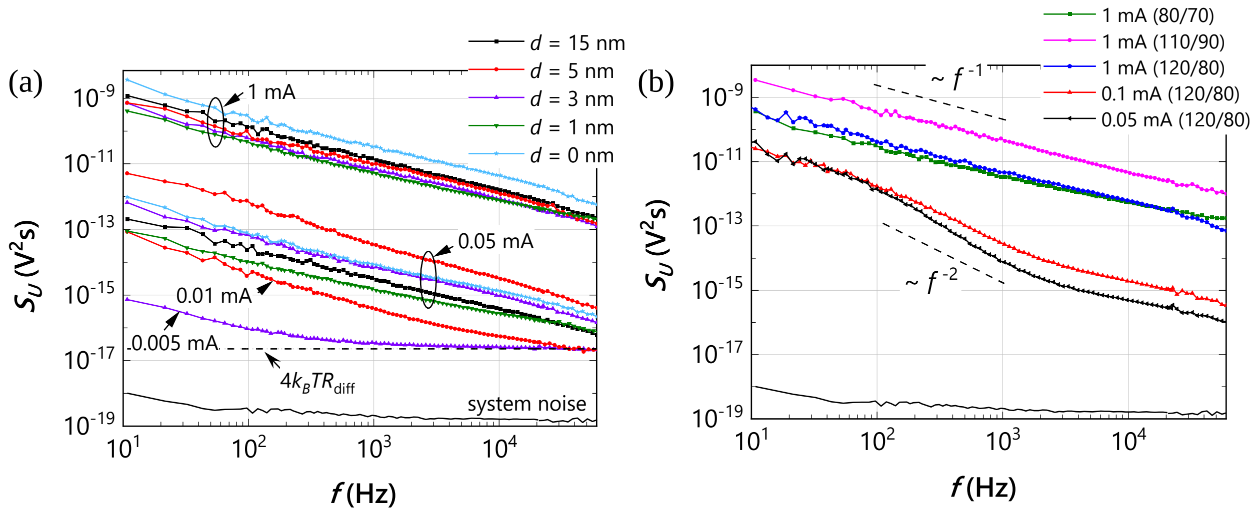


**Fig. A1.** Representative electrical noise spectra of investigated graphene/h-BN/Si (a) and hydrogenated graphene/Si (b) junctions at different reverse current values. The "system" represents the noise level of the measurement system; *d* – h-BN interlayer thickness. Numbers in brackets show $H_2/CH_4$ flow ratios used during hydrogenated graphene growth.

The dependences of the voltage noise spectral density on reverse bias current are similar across all investigated junctions (Fig. A2). At low reverse bias, the noise spectral density increases as $S_U \sim I^2$. This dependence is evident in the entire measured current range for samples with h-BN interlayer and reference junctions. In hydrogenated graphene/Si junctions, at high reverse bias, noise spectral density follows a cubic current dependence (Fig. A2 (b)), similar to that observed under forward bias conditions.

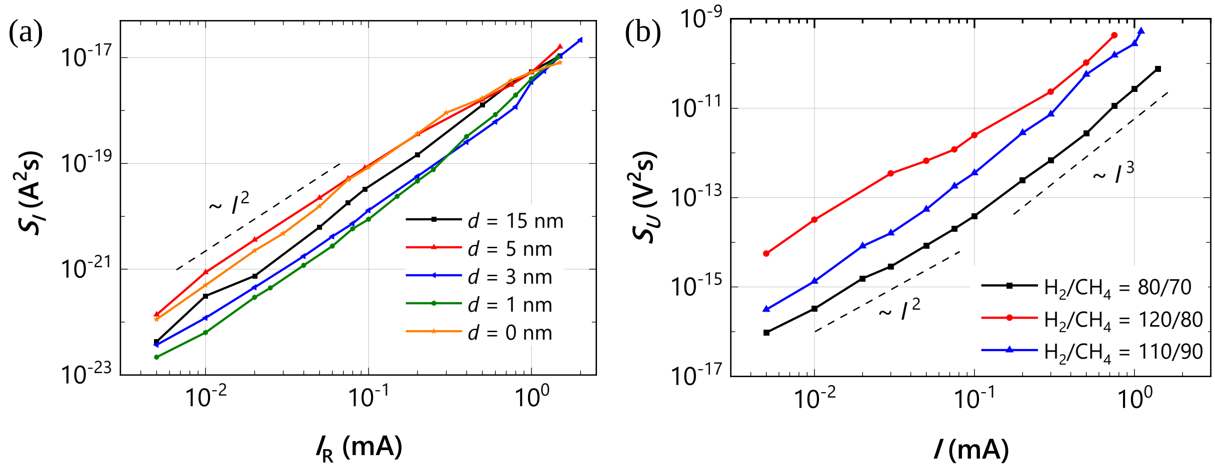


**Fig. A2.** Current noise spectral density dependencies on current of some investigated graphene/h-BN/Si samples (a) and voltage noise spectral density dependencies on current of hydrogenated graphene/Si samples (b) at reverse bias at $f$ = 108 Hz; $d$ – h-BN interlayer thickness.

## Conduction mechanisms in graphene/Si junctions

This section will discuss the observed conduction mechanisms in the investigated graphene/Si junctions.

Following the approach outlined in [62], the product of normalized current noise power spectral density $S_I/I^2$ and voltage $U$ (or electrical field) should be constant when plotted against current if Poole-Frenkel (PF) emission is the dominant charge transport mechanism in the device. Such behaviour has been noticed in samples with h-BN layer thicknesses of 15 nm and 5 nm at reverse bias (Fig. A3 (a)). A plateau in their corresponding plots is noticed at high bias, suggesting the dominance of PF emission. A trend is observed – samples with thicker h-BN layers are characterized by higher PF conductivity. This is clearly observed especially in the sample with 15 nm h-BN layer, where the plateau part is in a wide voltage range. The PF noise analysis at forward bias and high current was complicated due to the influence of grain boundaries on noise [7]. Only a few samples with 15 nm thickness h-BN layer demonstrate a narrow plateau in $U \times S_I/I^2$ vs. current plot at high forward bias (Fig. A3 (b)).

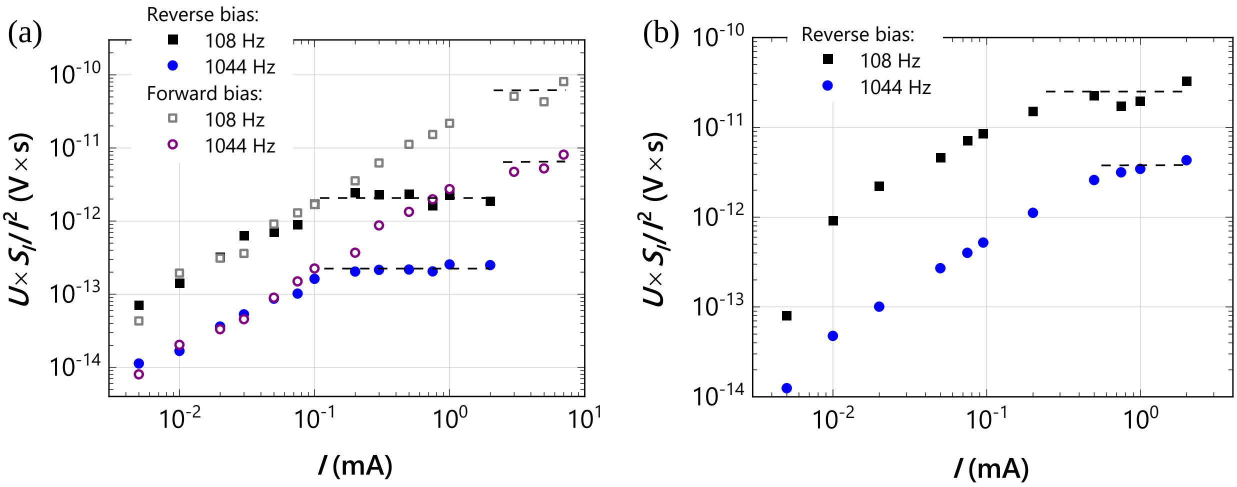


**Fig. A3.** $U \times S_I/I^2$ vs. current for 15 nm (a) and 5 nm (b) h-BN layer thickness samples at 108 Hz and 1044 Hz frequencies.

No PF emission has been observed in samples with hydrogenated graphene. Schottky emission is found in a narrow current interval in reference graphene/Si junctions and samples with hydrogenated graphene of group 1 ($H_2/CH_4$ = 80/70), as it was discussed earlier. However, different situation is observed in the remaining hydrogenated graphene/Si junctions. An example of the room temperature I-V characteristic of the group 2 junction is shown in Fig. A4 (a). The observed step-like bahaviour is generally indicative of a space charge limited conduction (SCLC) mechanism. With increasing current, a deviation from ohmic conduction becomes apparent. At ~ 0.7 V, defect states begin to fill because charge carriers are captured by traps, which are characterized by long relaxation times. Also, at approximately this voltage value a change in electrical noise type occurs – Lorentzian-type spectra emerge over the 1/*f* fluctuations (Fig. 15 (b)). At higher bias, the current exhibit dependence on voltage, $I \sim U^m$, where m ≈ 2, consistent with trap-filled SCLC process.

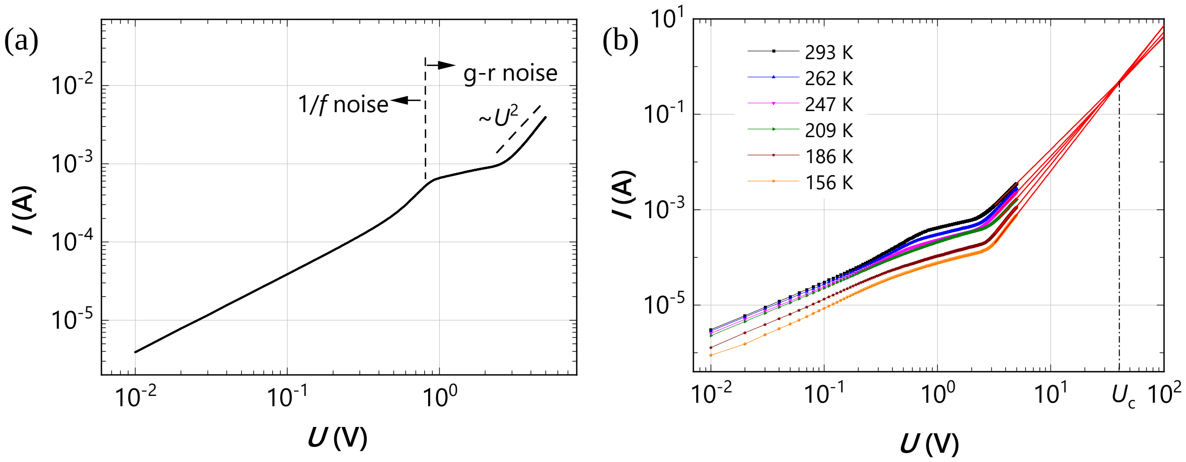


**Fig. A4.** I-V characteristics of a representative sample of group 2 ($H_2/CH_4$ = 110/90) at room temperature (a) and at different temperatures (b) at forward bias, $U_c$ – critical voltage.

Temperature dependent I-V measurements reveal that the index m changes from 2.3 at 293 K to m = 3.1 at 156 K (Fig. A4 (b)). A decrease in temperature leads to a reduction in free career density enhancing the influence of trap states. These temperature-dependent I-V curves are extrapolated and they intersect at a single point. According to the SCLC model [63], this point is referred to as the critical voltage $U_c$ and is expressed as:

$$U_c = \frac{qN_t d^2}{2\varepsilon_0 \varepsilon_r} \tag{18}$$

where $\varepsilon_0$ – the permittivity of free space, $\varepsilon_r$ – the dielectric constant of the material, $N_t$ – trap density, $d$ – spacing between electrodes. At the voltage $U_c$, the space-charge limited current is temperature independent. In group 2 samples critical voltage is 40 V [8].

## Graphene doping in gFETs

Pos(2D) downshift with a Pos(G) upshift (Fig. A5 (a)) shows n-type doping in graphene, according to the literature [4, 50]. Pos(2D) upshift with the *I*(2D)/*I*(G) ratio shows an increase in n-type self-doping of graphene with increasing thickness (Fig. A5 (b)) [4].

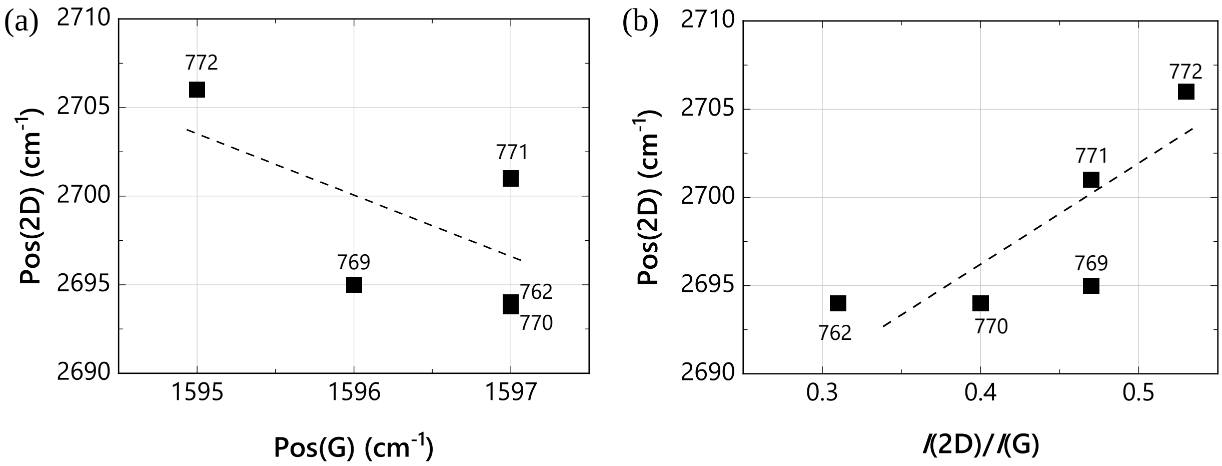


**Fig. A5.** Pos(2D) vs. Pos(G) plot (a) and Pos (2D) vs. *I*(2D)/*I*(G) ratio (averaged values) (b) of investigated gFETs. Lines are for an eye-guide only to represent the observed trends.

## References, only cited in Appendix:


[62] W. Shin, K. K. Min, J.-H. Bae, J. Yim, D. Kwon, Y. Kim, J. Yu, J. Hwang, B.-G. Park, D. Kwon, J.-H. Lee, "Comprehensive and accurate analysis of the working principle in ferroelectric tunnel junctions using low-frequency noise spectroscopy", *Nanoscale*, vol. 14, no. 6, pp. 2177–2185, 2022.

[63] D. Joung, A. Chunder, L. Zhai, S. I. Khondaker, "Space charge limited conduction with exponential trap distribution in reduced graphene oxide sheets", *Applies Physics Letters*, vol. 97, 093105, 2010.